Phase transition of WTAP regulates m^{6}A modification of interferon-stimulated genes

Sihui Cai[1,#], Jie Zhou[2,3,#], Xiaotong Luo[4], Chenqiu Zhang[1], Shouheng Jin[1], Jian Ren[4], Jun Cui[1]

[1] MOE Key Laboratory of Gene Function and Regulation, State Key Laboratory of Biocontrol, School of Life Sciences, Sun Yat-sen University, Guangzhou, Guangdong, 510006, China.

[2] State Key Laboratory of Membrane Biology & Frontier Research Center for Biological Structure, School of Life Sciences, Tsinghua University, Beijing, 100101, China.

[3] Tsinghua University-Peking University Joint Center for Life Sciences, Beijing, 100101, China.

[4] State Key Laboratory of Oncology in South China, Cancer Center, Collaborative Innovation Center for Cancer Medicine, School of Life Sciences, Sun Yat-sen University, Guangzhou 510006, China.

[#] These authors contributed equally: Sihui Cai, Jie Zhou.

Correspondence: Jun.Cui (cuij5@mail.sysu.edu.cn)

Abstract

N^6-methyladenosine (m^6A) is the most prevalent modification of mRNA which controls diverse physiological processes. Although m^6A modification has been reported to regulate type I interferon (IFN) responses by targeting the mRNA of IFN-β and the interferon stimulated genes (ISGs), the detailed mechanism of how m^6A methyltransferase complex (MTC) rapidly responds to conduct the modification on nascent mRNA during IFN-β stimulation remains largely unclear. Here, we demonstrate that WTAP, the adaptor protein of m^6A MTC, undergoes dephosphorylation-regulated phase transition from aggregates to liquid-like condensates under IFN-β stimulation, thereby mediates m^6A modification of a subset of ISG mRNAs to restrict their expression. The phase transition of WTAP promotes the interaction with nucleus-translocated transcription factor STAT1, which recruits MTC to the promoter regions of ISGs and directing the co-transcriptional m^6A modification on ISG mRNAs. Collectively, our findings reveal a novel regulatory role of WTAP phase transition in manipulating signaling pathways and fine-tuning immune response by orchestrating dynamic m^6A modification through the cooperation of transcription factors and MTC.

Keywords: m^6A modification, type I interferon, phase separation, WTAP, interferon-stimulated genes

Introduction

Innate immunity is the first defense line against invading pathogens, mainly through the induction of type I interferon (IFN) and IFN-stimulated genes (ISGs) (Goubau, Deddouche, & Reis e Sousa, 2013). Once the type I IFN is stimulated and initiated, the signal should be tightly restricted to maintain the homeostasis of immune responses (Henault et al., 2016; Schneider, Chevillotte, & Rice, 2014). In the past few years, a large number of studies have reported the post-translational modification of signaling proteins that regulate type I IFN signaling, such as phosphorylation (Uddin et al., 2002; Wen Z, Zhong Z, & Jr., 1995), ubiquitination (Cui et al., 2014; Qin et al., 2016) and methylation (Mowen et al., 2001). However, whether post-transcriptional modification of mRNA affects type I IFN responses remains largely unclear.

Methylation at the N^6 position of adenosine (m^6A) is the most pervasive post-transcriptional modification of mRNA. Deposition of m^6A is catalyzed by methyltransferase complex (MTC), including a key adaptor protein Wilm's tumor–associated protein (WTAP) and key catalyze proteins methyltransferase-like 3 (METTL3) and methyltransferase-like 14 (METTL14)(Schapira, 2016). The m^6A-modified RNAs are recognized by YT521B homology (YTH) domain family proteins, including YTHDC1, YTHDC2, YTHDF1, YTHDF2 and YTHDF3. m^6A modification have been found to regulate different cellular processes (Knuckles & Bühler, 2018; Meyer & Jaffrey, 2017), such as differentiation of stem cells (Geula et al., 2015), circadian clock (Zhong et al., 2018), splicing (Z. Zhang et al., 2010), translation (X. Wang et al., 2015) and destabilization of mRNA (X. Wang et al., 2014). Meanwhile, m^6A modification can be reversed by demethylase fat mass and obesity-associated gene (FTO) and AlkB homolog 5 (ALKBH5)(Jia et al., 2011; Zheng et al., 2013). m^6A modification is critical for newborn mRNA produced by specific stimulation to participate in further physiological activities. While m^6A modification of *IFN-β* mRNA suppresses antiviral responses during viral infection (Rubio, Depledge, Bianco, Thompson, & Mohr, 2018; Winkler et al., 2019), this modification also paradoxically enhances antiviral response through different regulation of ISG transcripts, such as enhancing translation of IFIT1 (McFadden et al.,

2021) and prolonging *STAT1* and *IRF1* mRNAs stability (L. Wang et al., 2020), demonstrating the complexity of m^6A in immune modulation. Given the crucial role of precise and timely m^6A modification on mRNA in fine-tuning antiviral responses, further investigation is required to clarify the function of non-catalytic protein WTAP and how MTC responds to IFN-β stimulation.

Here, we observed the phase transition from gel-like aggregates to liquid-like condensates of WTAP driven by IFN-β-induced dephosphorylation. Based on the results from the WTAP mutation assay, we revealed that under IFN-β stimulation, the liquid-phase of WTAP cooperated with transcription factor STAT1 to recruit MTC at the promoter regions of ISG, mediating the m^6A modification on newborn ISG mRNAs and regulated the expression of a subset of ISGs, thereby modulating antiviral type I IFN responses. Our study sheds light on the mechanism by which phase transition of WTAP bridges transcription factors and MTC to fine-tune m^6A deposition on specific mRNAs.

Results

WTAP undergoes phase separation during IFN-β stimulation

To explore the detailed mechanism of WTAP-directed m^6A modification on ISG mRNAs, we first investigated the expression of WTAP during virus infection. We infected cells with RNA virus Vesicular Stomatitis Virus (VSV) or DNA virus Herpes Simplex Virus-1 (HSV-1), and conducted the immunofluorescence experiments. Surprisingly, we found WTAP was clustered and formed condensate-like pattern in cells during virus infection (Figure 1A and Figure 1-figure supplement 1A). We then stimulated cells with IFN-β and observed the increasing number of WTAP condensates formation (Figure 1B). Previous studies have reported that some components in the methyltransferase complex such as METTL3 or YTHDFs undergo liquid-liquid phase separation (LLPS) during m^6A modification process (Han et al., 2022; J. Li et al., 2022). Therefore, we suspected whether the IFN-β-mediated WTAP condensates indicated phase separation.

A considerable number of proteins undergo phase separation via interactions between intrinsically disordered regions (IDRs). IDRs contain more charged and polar amino acids to present multiple weakly interacting elements, and lack hydrophobic amino acids to show flexible conformations(Hou et al., 2024). By searching WTAP protein structure (within part of MTC complex) in protein structure bank (https://www.rcsb.org/structure/7VF2), we found that WTAP IDR was predicted to span amino acids from 245 to 396, giving a clue that WTAP might have the ability to undergo phase separation (Figure 1C). To directly prove the phase separation properties of WTAP *in vitro*, we purified the recombinant mCherry-WTAP protein, mixed recombinant mCherry-WTAP with physiological buffer and found that the buffer became turbid (Figure 1D). Observation under microscope showed that mCherry-WTAP automatically formed liquid-like condensates which could be reversed by 1,6-hexanediol (hex), an inhibitor of phase separation (Figure 1E). Phase diagram of WTAP phase separation was also established under different concentrations of potassium chloride and recombinant mCherry-WTAP (Figure 1-figure supplement 1B). Fusion of condensates were observed and larger condensates were formed *in vitro* (Figure 1-figure supplement 1C). These data together confirmed that WTAP underwent phase separation *in vitro*.

To further explore the protein properties, we detected the phase separation behavior of WTAP in cells. Gene expressing mCherry-WTAP was introduced in WTAP-KO HeLa cells to generate mCherry-WTAP-rescued HeLa cells, followed with IFN-β stimulation. A few WTAP condensates were discovered in untreated cells while an increasing number of WTAP condensates were observed under IFN-β stimulation. After hex treatment, WTAP condensates in IFN-β treated cells dissipated into a dispersed pattern (Figure 1F). Similarly, hex treatment in virus-infected cells also disrupted the formation of WTAP condensates (Figure 1A and Figure 1-figure supplement 1A). We next checked the mobility of WTAP condensates by fluorescence recovery after photobleaching (FRAP) experiments. Intriguingly, WTAP exhibited lower recovery intensity in untreated cells but higher mobility with rapid recovery intensity in IFN-β-treated cells (Figure 1G). These results suggested a

potential dynamic transformation in WTAP phase separation. While WTAP underwent gel-like phase separation under basal conditions, IFN-β induced its phase transition to form the liquid-like condensates under physiological conditions.

Previous studies have uncovered that protein phase separation could be controlled by interaction between specific regions through multiple factors (Murthy et al., 2019; J. Wang et al., 2018), including electrostatic interactions (Boyko, Qi, Chen, Surewicz, & Surewicz, 2019), hydrophobic contacts (Reichheld, Muiznieks, Keeley, & Sharpe, 2017) or hydrogen bonds (Gabryelczyk et al., 2019). Therefore, we tried to figure out the phase separation-driven region of WTAP. We analyzed the net charge per region and hydropathy of WTAP, but no specific domains with opposite charge or high level of hydrophobicity were found (Figure 1-figure supplement 2A-B), indicating that electrostatic interaction and hydrophobic contacts might not be the key driving force for WTAP phase separation. We then analyzed the abundance of amino acids and found that Serine (Ser), Glutamine (Gln), Glutamate (Glu) and Leucine (Leu) were present at significantly higher levels than other amino acids within WTAP (Figure 1C and Figure1-figure supplement 2C). Gln and Leu were mainly located in the N-terminal domain (NTD) while Ser was mostly enriched in the C-terminal domain (CTD), implying the different properties of NTD and CTD (Figure 1C). Notably, IDR of WTAP were predicted to cover the entire serine-rich CTD region. Previous researches reported that hydrogen bond between serine side chain mediated the intermolecular interaction and LLPS of FUS. In addition, abnormal glutamine-repeat resulted in the formation of β-sheet and solid/gel-like aggregates with lower mobility (Perutz, 1996; Tanaka, Morishima, Akagi, Hashikawa, & Nukina, 2001), which were related to neurodegenerative diseases like Huntington's disease (Gourfinkel-An et al., 1997). Therefore, we wondered whether glutamine-rich NTD and serine-rich CTD of WTAP induced the distinct phase separation. As predicted, we found full-length WTAP and CTD WTAP formed liquid condensates, while NTD of WTAP clustered and formed aggregates with lower mobility, which was confirmed through FRAP experiments (Figure 1H and Figure 1-figure supplement 2D). Intriguingly, we further observed that full-length WTAP transited from liquid-like condensates to aggregates

after incubation for several minutes while CTD of WTAP remained liquid phase (Figure 1-figure supplement 2E). Collectively, these data validated the different phase separation potential of NTD and CTD of WTAP.

IFN-β-mediated dephosphorylation induces the phase transition of WTAP

Since the serine-rich CTD played the key role in liquid condensates formation of WTAP, we wondered whether IFN-β-mediated WTAP phase transition through serine-phosphorylation by electrostatic repulsion among negatively charged phosphate. We first detected the phosphorylation level of WTAP through immunoprecipitation (IP) assay and found that phosphorylation of WTAP was significantly decreased under IFN-β stimulation (Figure 2A). Through IP assays, we aimed to identify the phosphatases that dephosphorylate WTAP, thus checked the interaction between WTAP and family of protein phosphatases (PPPs), and found that PPP4 presented the strongest interaction with WTAP (Figure 2-figure supplement 1A). IFN-β stimulation promoted the interaction between WTAP and PPP4 (Figure 2B and Figure 2-figure supplement 1B). Both knockdown of *PPP4* and the potent PPP4 inhibitor fostriecin restrained the dephosphorylation of WTAP in IFN-β treated cells (Figure 2C). Potent PPP4 inhibitor fostriecin to detect, which significantly impaired the IFN-β-induced dephosphorylation of WTAP (Figure 2-figure supplement 1C). These data indicating that IFN-β regulated dephosphorylation of WTAP through PPP4.

To validate the effects of phosphorylation on the phase transition of WTAP, we first confirming the phosphorylation site of WTAP by mass spectrometry (MS) assays. MS results identified six phosphorylated serine/threonine sites within WTAP, while five of six phosphorylation sites were located in CTD of WTAP (Figure 2D and Figure 2-figure supplement 1D). We then constructed a series of phosphorylation mimic, serine/threonine to aspartate mutants (S/T-D) or phosphorylation-deficient, serine/threonine to alanine mutant (S/T-A) of WTAP, and observed the phase separation of WTAP mutants *in vitro*. We found that introducing three or more phosphorylation-mimic mutations in WTAP promoted protein aggregation (Figure 2E

and Figure 2-figure supplement 1E). While the 5ST-D mutant induced aggregation, the 5ST-A mutant formed liquid condensates comparable to wild-type (WT) WTAP, which remained unphosphorylated in the E. coli expression system lacking endogenous kinase activity (Figure 2F). We next conducted FRAP experiments and found that mobility of WT WTAP as well as 5ST-A was significantly higher than that of its 5ST-D mutant *in vitro* (Figure 2G). However, hyperphosphorylated WT WTAP in untreated cells showed lower mobility as 5ST-D mutant compared to phosphorylation-deficient 5ST-A mutant, while IFN-β-induced dephosphorylation promoted the recovery efficiency of WT WTAP as higher as 5ST-A mutants of WTAP (Figure 2H). Additionally, we found the liquid condensates of WTAP after IFN-β stimulation was blunted in *PPP4* knocked-down cells and fostriecin treatment (Figure 2-figure supplement 1F-H), revealed that IFN-β triggered PPP4-mediated dephosphorylation of WTAP controlled the phase transition of WTAP. Taken together, we validated hyperphosphorylation of WTAP tended to form aggregates with low mobility due to electrostatically repulsed between phosphorylated serine sites, while hypophosphorylation of WTAP promoted the mobility and forms liquid condensates. IFN-β-mediated dephosphorylation promotes the transition from aggregates to liquid-phase of WTAP both *in vitro* and in cells (Figure 2I).

Phase transition of WTAP directs m^{6}A modification on ISG mRNAs to regulate ISGs expression

Next, we aimed to determine how IFN-β-mediated WTAP phase transition functioned in ISG mRNAs. Previous reports have shown that m^{6}A modification affected antiviral activity through ISG mRNAs stabilization or translation (McFadden et al., 2021; L. Wang et al., 2020). To verify the function of WTAP on ISG mRNAs m^{6}A modification, we generated *WTAP*^{sgRNA} THP-1 cells using the CRISPR-Cas9 system, and performed RNA sequencing (RNA-Seq) followed with bioinformatic analysis, and uncovered that 1,440 and 1,689 genes were up-regulated in response to IFN-β stimulation for 6 and 12 hours respectively (Figure 3A-B and Figure 3-figure supplement 1A). Among this, 441 ISGs exhibited elevated expression in *WTAP*^{sgRNA}

cells, including *IFIT1*, *IFIT2*, *OAS1* and *OAS2*, which were enriched in various immune-related pathways (Figure 3C-D and Figure 3-figure supplement 1B). We also found that WTAP showed no effect on both the expression level and the phosphorylation level of transcription factors STAT1, STAT2 and IRF9 under IFN-β stimulation (Figure 3-figure supplement 1C-D), suggesting that changes of WTAP-regulated changes in ISGs expression were independent of phosphorylation level of indicated transcription factors.

We then collected the mRNA of control and *WTAP*^{sgRNA} cells stimulated with or without IFN-β to perform m^{6}A methylated RNA immunoprecipitation followed by deep sequencing (MeRIP-Seq). Consensus m^{6}A modified core motifs were enriched in our samples and the majority of WTAP-dependent m^{6}A modification peaks were located in coding sequences (CDS) and 3'- untranslated regions (UTR) (Figure 3E-F and Figure 3-figure supplement 1E-F). A group of ISGs that was m^{6}A modified in control cells but showed diminished modification in *WTAP*^{sgRNA} cells were clustered in the IFN-associated pathway through MeRIP-seq assays, verifying the WTAP-dependent m^{6}A modification of ISG mRNAs during IFN-β stimulation (Figure 3-figure supplement 1G). Notably, around 64.29% of core ISGs and 61.90% of WTAP down-regulated ISGs were m^{6}A modified, which was consistent with the similar percentage in previous studies (McFadden et al., 2021; Winkler et al., 2019) (Figure 3G and Figure 3-figure supplement 1B). The topology of ISGs m^{6}A sites was analyzed, revealing a strong preference for CDS localization compared to global m^{6}A deposition (Figure 3H and Figure 3-supplement 1H). MeRIP-quantitative real time-polymerase chain reaction (qPCR) assays confirmed the reduced m^{6}A modification level on WTAP-down-regulated ISGs, including *IFIT1*, *IFIT2*, *OAS1* and *OAS2* (Figure 3I). Given that m^{6}A deposition was reported to affect various aspects of RNA, especially for the decay of mRNA (Oerum, Meynier, Catala, & Tisne, 2021; Shi et al., 2017; X. Wang et al., 2014), we also checked the mRNA stabilization by inhibiting synthesis of nascent mRNA using Actinomycin D (Act D), and the expression level of these ISGs by qPCR assay. Our results showed that WTAP deficiency stabilized ISG mRNAs, leading to their up-regulated expression (Figure 3J-K).

To further delineate the function of WTAP phase separation on m^6A modification, we treated cells with hex to disrupt the phase separation of WTAP, and detected the m^6A deposition in cells with virus infection or IFN-β treatment. We found that virus infection or IFN-β stimulation induced m^6A modified ISG mRNAs, and their m^6A modification was disrupted by phase separation inhibitor hex (Figure 4A and Figure 4-figure supplement 1A-B). Hex increased ISG mRNAs stability in control cells but had no effect in *WTAP*^{sgRNA} cells, suggesting WTAP phase separation was essential for ISG mRNAs m^6A deposition and stabilization (Figure 4-figure supplement 1C). Next, we aimed to uncover the distinct ability to direct m^6A modification of ISGs between aggregates or liquid-phase separated WTAP. Knockdown of *PPP4* or treatment with its inhibitor fostriecin, maintained WTAP in a hyperphosphorylated and aggregated status under IFN-β stimulation, and the m^6A modification level on ISG mRNAs were surprisingly found to be decreased (Figure 4B-C). Enhanced mRNA level was also detected with PPP4 deficiency or inhibition (Figure 4-figure supplement 1D-E). We re-introduced WT WTAP, or its 5ST-D or 5ST-A mutant into *WTAP*^{sgRNA} THP-1 cells to generate WT WTAP, 5ST-D or 5ST-A THP-1 cells respectively (Figure 4-figure supplement 1F). Our results showed that m^6A modification level of ISG mRNAs in *WTAP*^{sgRNA} and WTAP 5ST-D mutant cells was significantly attenuated than that of control cells, WT WTAP cells and WTAP 5ST-A mutant cells (Figure 4D). Hex suppressed m^6A modification in WT WTAP and 5ST-A cells, but not in 5ST-D cells, implying the crucial role of liquid-phase separated WTAP in m^6A deposition event (Figure 4E). Taken together, these results demonstrated that m^6A modification of ISG mRNAs was mainly regulated by the liquid-phase separated WTAP dephosphorylated by PPP4 under IFN-β stimulation.

Liquid-phase separated WTAP recruits MTC and STAT1 on promoter regions to direct the m^6A modification of ISG mRNAs

Although m^6A modification of ISGs has been reported previously, the detailed mechanism of how WTAP directed m^6A modification on ISG mRNAs and the distinct mechanism between WTAP aggregates and liquid-phase separated WTAP were still

unknown. By analyzing expression levels of WTAP and other m^6A methylation complex proteins, no significantly alteration were observed during 6 hours of IFN-β stimulation (Figure 5-figure supplement 1A-B). By MeRIP-seq, we discovered the m^6A modification sites of ISGs were preferentially localized to CDS region (Figure 3H), which aligned with co-transcriptional m^6A patterns (Barbieri et al., 2017; H. Huang et al., 2019). Additionally, previous researches have demonstrated the interaction between METTL3/WTAP and the transcription factor STAT5B and SMAD2/3 directed m^6A modification to downstream genes, supporting transcription factors-mediated co-transcriptional m^6A modification (Bertero et al., 2018; Bhattarai, Kim, Lim, & Choi, 2024) . Therefore, we wondered whether m^6A modification of ISG mRNAs was directed co-transcriptionally by WTAP and IFN-β-activated transcription factors, including STAT1, STAT2 and IRF9(Schneider et al., 2014). Occupancy of the promoters of WTAP-regulated ISGs (2000 bp upstream of genes were analyzed, while 500 bp upstream of genes were considered as the proximal part of promoter) were predicted through directing using AnimalTFDB 3.0 website (http://bioinfo.life.hust.edu.cn/AnimalTFDB/) (Hu et al., 2019). Most of the ISGs were occupied by STAT1 rather than STAT2 and IRF9 (Figure 5A), especially for the proximal part of promoter, pointing the possible role of STAT1 in WTAP-induced m^6A modification. We then detected the interaction between WTAP, METTL3 and STAT1 through IP assay and found that the interaction between WTAP, METTL3 and nuclear-translocated STAT1 was enhanced under IFN-β stimulation (Figure 5B, and Figure 5-Figure supplement 1C). Additionally, the interaction between STAT1 and METTL3 was abolished in *WTAP*^{sgRNA} cells (Figure 5C). RIP-qPCR assays confirmed disrupted METTL3-ISG mRNAs interaction in *WTAP*^{sgRNA} cells, demonstrating the involvement and importance of WTAP in METTL3-dependent m^6A deposition, and verifying the formation of STAT1-WTAP-METTL3-ISG mRNAs complex under IFN-β stimulation (Figure 5D).

To assess the contribution of phase-separated WTAP, we used hex to disrupt WTAP phase separation, and interaction with STAT1 were analyzed. The interaction between WTAP, METTL3 and STAT1 was dramatically inhibited with hex treatment

both in cells and *in vitro* (Figure 5E-F, and Figure 5-figure supplement 1D). By immunofluorescence (IF) experiments, we found IFN-β promoted the interaction between WTAP, METTL3 and nuclear-translocated STAT1 in cells, which could be abolished by hex (Figure 5G). The interaction between WTAP, METTL3 and STAT1 were enhanced in the liquid-phase mutant WTAP 5ST-A rescued cells, which could be impaired by hex treatment (Figure 5-figure supplement 1E). The condensation among recombinant GFP-STAT1, mCherry-WTAP and CFP-METTL3 *in vitro* were detected, and observed that WTAP was able to form condensates with STAT1 or METTL3 alone while condensation of STAT1 and METTL3 was significantly diminished in the absence of WTAP (Figure 5H-I and Figure 5-figure supplement 1F). Consistent with the results in cells, the interaction between WTAP and STAT1 was blunted by hex (Figure 5-figure supplement 1G). Notably, both 2% and 5% hex did not alter the PPP4c-mediated WTAP dephosphorylation level, confirming that hex inhibited WTAP phase separation but not its de-phosphorylation event (Figure 5-figure supplement 1H). Altogether, our data showed that phase separated WTAP functioned as the key adaptor protein bridging METTL3 and STAT1 to direct the m^6A modification of ISG mRNAs.

We next tried to figure out how STAT1-MTC bound and mediated m^6A modification on ISG mRNAs. By performing the chromosome immunoprecipitation (ChIP)-qPCR experiments, we found that WTAP interacted with promoter regions of ISGs along with STAT1 under IFN-β stimulation (Figure 6A-B). STAT1 deficiency abolished the binding affinity between WTAP and ISG promoter regions (Figure 6C), implying that nucleus-translocated transcription factor STAT1 directed WTAP and MTC to promoter regions of ISGs to conduct m^6A deposition process on mRNA. *PPP4* knockdown impaired interaction between WTAP and ISG promoter region, linking the interaction efficiency to phase transition of WTAP (Figure 6C). WTAP 5ST-D mutant THP-1 cells exhibited significantly reduced binding ability with ISG promoter regions compared to WT WTAP and 5ST-A mutant THP-1 cells after IFN-β stimulation (Figure 6D), which consistent with the m^6A modification results (Figure 4D). Hex treatment also restrained the interaction between WTAP and ISGs

promoter regions in WT WTAP and WTAP 5ST-A cells (Figure 6E), consistent with the m^6A modification results (Figure 4E). Collectively, WTAP phase separation was important for the promoter regions targeting and subsequent m^6A deposition on ISG mRNAs.

Taken together, our findings revealed the driving force of aggregation and liquid condensates formation of WTAP, and demonstrated the distinct function between aggregates and liquid-phase separated WTAP. Based on our findings, we proposed a working model of WTAP phase transition in the regulation of m^6A modification of ISG mRNAs under IFN-β stimulation. In untreated cells, hyperphosphorylated WTAP tended to form gel-like aggregates with lower mobility, restricting interaction between WTAP-dependent MTC and ISG promoter region. After IFN-β stimulation, protein phosphatase PPP4 mediated the dephosphorylation of WTAP, resulting in the phase transition from aggregates to liquid-phase of WTAP. Liquid-phase WTAP exhibited enhanced mobility, recruiting METTL3 and nucleus-translocated STAT1 to form STAT1-WTAP-METTL3 condensates. Guided by STAT1, these condensates were able to bind with ISG promoter regions and mediate the m^6A modification of ISG mRNAs during the STAT1-driven transcription process, thereby prompting diverse regulation on stability of ISG mRNAs. Our work uncovered how WTAP phase transition couples gene transcription with mRNA modification, providing a novel mechanism on multi-layer regulation of ISGs expression via m^6A modification (Figure 6F).

Discussion

Type I IFN response is a crucial part of the antiviral immunity, which is strictly controlled by various types of regulation to avoid unexpected tissue damages. m^6A deposition is one of the most widespread post-transcriptional modifications, which is involved in various aspects of RNA metabolism to regulate different biological events, including antiviral response (Garcias Morales & Reyes, 2021). m^6A deposition on IFN-β mRNA is reported to dampen type-I IFN production by destabilizing transcripts, yet no m^6A is detected on ISG mRNAs in the same study

(Winkler et al., 2019). Subsequent works, however, reveal the diverse effects on antiviral responses mediated by the m^6A modification of ISG mRNAs. hnRNPA2B1-dependent m^6A modification of *cGAS*, *IFI16* and *STING* promotes their nuclear exportation to amplify the cytoplasmic innate sensor signaling, while METTL3/METTL14-mediated m^6A modification on IFITM1 and MX1 up-regulates their translation efficiency to positively regulate the antiviral response (McFadden et al., 2021; McFadden et al., 2022; L. Wang, Wen, & Cao, 2019). Conversely, m^6A modification destabilizes IRF7 mRNA to suppress antiviral responses (A. Wang et al., 2022). Virus hijacks MTC components (e.g., WTAP degradation) to suppress the translational of *IRF3* and stability of *IFNAR1* mRNA via reduced m^6A deposition, thereby exacerbating antiviral dysregulation (Ge et al., 2021). In our study, we employed IFN-β treatment to avoid the influence of m^6A modification-mediated IFN-β mRNA decay, experimentally validated m^6A deposition on a subset of ISG mRNAs fine-tunes antiviral responses by reducing transcript stability, maintaining a steady antiviral response and alleviates the hyper-activation of IFN-β signaling. Our findings together demonstrated the diverse function of m^6A modification on ISG mRNAs, including suppression of transcription, promotion of translation, regulation of mRNA stabilization or even the cellular trafficking of mRNA, highlighting the complexity of m^6A modification in mRNA fate determination, and emphasizing the needs of precise regulation on immune response.

WTAP, a core scaffolding protein of MTC, recruits and stabilizes other MTC components, such as METTL3 and METTL14, into nuclear speckles. Abnormal expression of WTAP is discovered in multiple diseases, including cancer or diabetes, to address dysfunctional m^6A modification in specific genes (Chen et al., 2019; Q. Huang, Mo, Liao, Chen, & Zhang, 2022; Z. X. Li et al., 2022; Yu et al., 2021). However, how WTAP reacts in response to specific stimulation and selectively targets specific mRNA remains unclear. Here, we focused on the function of WTAP on antiviral response, uncovered the novel mechanism that WTAP underwent IFN-β-induced dephosphorylation-mediated gel-to-liquid phase transition, which mediated

its interaction with transcription factor STAT1, directing MTC to conduct the m^6A modification on nascent ISG mRNAs co-transcriptionally.

Phase separation is a well-known phenomenon associated with the formation of membraneless organelles, which concentrates the substrates and enzymes and accelerates biochemistry reactions (Alberti, Gladfelter, & Mittag, 2019). Previous researches uncover the involvement of phase separation in m^6A modification process, METTL3 and YTHDFs undergo LLPS during the m^6A deposition and recognition process (Han et al., 2022; J. Li et al., 2022), and m^6A modification promotes the LLPS of RNA-binding proteins, including m^6A-mRNA-YTHDFs and m^6A-eRNA/YTHDC1/BRD4 condensates (Gao et al., 2019; Lee et al., 2021; Ries et al., 2019; J. Wang et al., 2020). However, whether other MTC components exhibits phase separation is still unknown. Here, we observed that WTAP also went through phase separation both *in vitro* and *in vivo.* We found WTAP mainly formed the aggregates with lower mobility in untreated cells, and transited to liquid condensates with IFN-β treatment, implying that phase separation participated in WTAP-dependent m^6A deposition under IFN-β stimulation. We found hex treatment or phospho-mimic mutations (5ST-D) trapped WTAP in low-mobility aggregates, impairing ISG promoter binding and m^6A deposition. These results uncovered the mechanism and the crucial role of WTAP phase separation and phase transition in MTC assembly and ISGs m^6A deposition under IFN-β stimulation. Furthermore, the phase transition of WTAP suggested a potential mechanism that aggregation of WTAP might work as a backup storage, and the stimuli-induced phase transition was developed to perform the m^6A modification timely and precisely in response to the requirement of cell development or abnormal situations. Thus, investigation of WTAP phase separation in different model could be conducted to explain the mechanism of m^6A modification under complex stimulation and explore possible therapeutic targets of multiple diseases.

Post-translational modifications are one of the most common ways to modulate characteristic of proteins (Y. Y. Luo, Wu, & Li, 2021), like phosphorylation of serine and threonine (Markevich, Hoek, & Kholodenko, 2004) and methylation of arginine

(Guccione & Richard, 2019). Several reports indicate that phosphorylation of phase-separated proteins are associated with the solid/gel-like aggregates formation or solid/gel-to-liquid phase transition, participating in various physiological process such as the pathogenesis of tau protein aggregates or acute transcriptional response (Arendt, Stieler, & Holzer, 2016; Boyko et al., 2019; H. Zhang et al., 2022), but whether the phosphorylation-controlled phase transition of proteins regulate other physiological process remains to be illustrated. In this study, we observed PPP4-mediated dephosphorylation of WTAP at serine/threonine residues triggered a gel-to-liquid phase transition, enabling STAT1-MTC recruitment. Consistently, phosphomimic 5ST-D mutant of WTAP mainly aggregated as lower mobility form compared to phosphodeficient 5ST-A mutant of WTAP, which formed liquid condensates in cells, indicating that phosphorylation level of WTAP balanced its phase transition. Therefore, our findings shed light on the mechanism of post-translational modification-regulated phase transition of WTAP and put forward an open question whether phosphorylation and other post-translational modifications function as the key strategy for global phase transition of proteins *in vivo*.

Since we found the phase transition event of WTAP and its interaction with transcription factor STAT1, we proposed that co-transcriptional m^6A modification on nascent ISG transcripts might occur during IFN-β stimulation. As a global modification in cells, m^6A modification can be hindered by MTC along with the inhibition role of exon junction complex, lead to the specificity of modification, mapping the m^6A topology and maintain in stable state (He et al., 2023; Z. Luo et al., 2023; Uzonyi et al., 2023; Yang, Triboulet, Liu, Sendinc, & Gregory, 2022). More and more results suggest that MTC can be recruited by methylated histone proteins or transcription factors, enrich in different chromatin loci, such as promoter, to dynamically deposit m^6A modification on nascent mRNA co-transcriptionally under certain circumstance or function in various physiological activities, implying the importance of interaction between MTC and chromatin architecture (Dou et al., 2023; Sendinc & Shi, 2023; Xu et al., 2022). Transcription factor SMAD2/3, STAT5B, KLF9 and CEBPZ are found to recruit MTC on transcriptional start sites (TSS) and

specifically direct the m^6A modification on a subset of downstream transcripts mRNA CDS region, thereby affecting the cell fate decision (Barbieri et al., 2017; Bertero et al., 2018; Bhattarai et al., 2024). In line with this, we validated that the IFN-β-induced WTAP-STAT1 interaction guided MTC to the promoter regions of ISGs to direct the m^6A modification on ISG mRNAs. We also revealed that the WTAP-mediated m^6A modification of ISG mRNAs mainly occurs within the coding regions, different from its distribution in the general transcriptome that enriched within mRNA 3'-UTR. Our findings raised a novel perspective that transcription factor-MTC interaction directed co-transcriptional m^6A modification to balance immune activation and homeostasis.

Taken together, our study drew a full picture of the phase transition of WTAP and the function of STAT1- MTC directed m^6A modification on ISG mRNAs under IFN-β stimulation. Our findings unraveled a novel mechanism of fine-tuning m^6A methylated mRNA profile under stimulation, and provided a possible therapeutic target in antiviral responses and many other diseases.

Materials and Methods

Cells.

THP-1 cells obtained from the Cell Bank of the Chinese Academy of Sciences (Shanghai, China) were cultured in RPMI 1640 (Gibco) with 10% (vol/vol) fetal bovine serum (FBS), 1% penicillin-streptomycin (Gibco,1:100) and 1% L-glutamine (Gibco) incubated in a 37°C chamber with 5% CO_2 (Thermo Fisher Scientific). Before stimulation, THP-1 cells were differentiated into macrophages (THP-1-deirived macrophages) through treatment of 100 nM phorbol-12-myristate-13-acetate (PMA) (P8139, Sigma) for 16 hours. After PMA treatment, the macrophages were rested for 48 hours before stimulation. A549 and HeLa cells obtained from the Cell Bank of the Chinese Academy of Sciences (Shanghai, China) were cultured in DMEM medium (Corning) with 10% FBS and 1% L-glutamine (Gibco) incubated in a 37°C chamber with 5% CO_2.

Reagents and Antibodies.

IFN-β (cat. #300-02BC) was purchased from PeproTech Inc. PMA (cat. #P1585), puromycin (cat. #P9620), Actinomycin D (cat. #SBR00013), 1,6-hexanediol (cat. #240117), digitonin (cat. #D141), DTT (cat. #3483-12-3), DAPI (cat. #D9542) were purchased from Sigma-Aldrich. Fostriecin (cat. #ab144255) was purchased from Abcam. Isopropyl-beta-D-thiogalactopyranoside (IPTG, cat. #CA413) and Superluminal High- efficiency Transfection Reagent (cat. # 11231804) were purchased from MIKX. Hieff-Trans Liposomal Transfection Reagent (40802ES02) were purchased from Yeasen. NP-40 (cat. #P0013F) was purchased from Beyotime Biotechnology. The antibodies that used in this study were listed in *Supplementary Appendix, Table S1*.

Generation of knockout cell lines by CRISPR/Cas9.

After THP-1 cells were seeded, medium was replaced by DMEM containing polybrene (8 μg/ml) (Sigma-Aldrich) lentiviral vector encoding Cas9 and small guide RNAs (sgRNA) for 48 hours. Cells were selected using puromycin (Sigma-Aldrich). The sequence of sgRNAs targeting indicated gene obtained from Sangon (Shanghai, China) were listed in *Supplementary Appendix, Table S2*:

siRNA Transfection.

siRNA duplexes and scrambled siRNA were chemically synthesized by RIBOBIO (Guangzhou, China) and transfected into cells using LipoRNAiMAX reagent (Invitrogen) according to the manufacturer's instructions. The sequences of siRNAs were listed in *Supplementary Appendix, Table S2*:

Virus infection.

VSV and HSV-1 were amplificated and tittered on Vero E6 cell line. Virus titers were measured by means of 50% of the tissue culture's infectious dose (TCID50). Virus were infected into indicated cell lines with indicated titers as shown in figure legends.

Immunoblot (IB) assays and immunoprecipitation (IP).

Relevant cells were stimulated as indicated, and whole cell lysate was obtained using low-salt lysis buffer (50 mM Hepes (pH 7.5), 150 mM NaCl, 1 mM EDTA, 1.5 mM $MgCl_2$, 10% glycerol, 1% Triton X-100, supplemented with protease inhibitor cocktail (cat. #A32965, Pierce) and phosSTOP Phosphatase Inhibitor Cocktail (cat. #4906837001, Roche)). Cell lysates were centrifuged at 4°C, 12000 g for 15 minutes and supernatants was boiled at 100 °C for 5 minutes with the 5×Loading Buffer (cat. #FD006, Hangzhou Fude Biological Technology Co, LTD.). Solution was resolved by SDS-PAGE, transferred to polyvinylidene fluoride (PVDF) membranes (cat. #1620177, Bio-Rad Laboratories, Inc.), blocked with 5% skim milk (cat. #232100, BD) for 1 hour and incubated with appropriate antibody. Immobilon Western HRP Substrate (cat. #WBKLS0500, Millipore) was used for protein detection with ChemiDoc MP System (Bio-Rad Laboratories, Inc.) and Image Lab version 6.0 (Bio-Rad software, California, USA). For immunoprecipitation, protein samples were incubated with protein A/G beads (cat. #20333, #20399, Pierce) or anti-Flag M2 affinity gel (cat. #A2220, Sigma-Aldrich) together with indicated antibody at 4°C overnight. Beads were washed five times with low-salt lysis buffer and boiled at 100 °C for 5 minutes with 2×SDS loading buffer, followed with immunoblot assays described above.

Mass spectrometry.

HEK 293T cells were transfected with plasmids expressing mCherry-WTAP. 24 hours after transfection, whole cell lysate was obtained using low-salt lysis buffer and immunoprecipitated using protein A/G beads together with anti-WTAP antibody at 4°C overnight. Proteins were obtained from beads and analyzed by LC-MS/MS analysis. Details were shown in *Supplementary Appendix, Extended Methods*.

RNA extraction, quantitative real-time polymerase chain reaction (qPCR) and RNA sequencing (RNA-Seq) assay.

Relevant cells were treated as indicated and total RNA was extracted from cells with

TRIzol reagent (cat. #15596026, Invitrogen), according to the manufacturer's instructions. RNA was then reverse-transcribed into cDNA using HiScript® III RT SuperMix for qPCR (+gDNA wiper) (cat. #R323-01, Vazyme). The level of indicated genes were determined by qPCR with 2×PolarSignal™ SYBR Green mix Taq (cat. #MKG900-10, MIKX) using LightCycler® 480 System (Roche). The primers used in qPCR were listed in *Supplementary Appendix, Table S2*. For RNA-Seq assay, total RNA was isolated from cells using TRIzol reagent, and sequencing was performed by Sangon Biotech (Shanghai, China). Details of RNA-Seq data analysis were shown in *Supplementary Appendix, Extended Methods*.

Chromatin-immunoprecipitation (ChIP) assay.

THP-1 cells were treated as indicated and DNA were enriched through ChIP assay referred to the Rockland Chromatin Immunoprecipitation assay protocol. Details were shown in *Supplementary Appendix, Extended Methods.* After ChIP enrichment, DNA were analyzed through qPCR assay. The sequences of primers were listed in *Supplementary Appendix, Table S2*:

RNA-immunoprecipitation (RIP) followed with qPCR assay.

THP-1 cells were treated as indicated and RNA were enriched through RIP assay referred to the previously reported protocol (Keene, Komisarow, & Friedersdorf, 2006). Details were shown in *Supplementary Appendix, Extended Methods*. After RIP enrichment, RNA was analyzed through qPCR assay. The sequences of primers were listed in *Supplementary Appendix, Table S2*:

m^6A methylated RNA immunoprecipitation (MeRIP) followed with qPCR assay and MeRIP-Seq assay.

For MeRIP-qPCR, the procedures were referred to the protocol as manufacturer's instructions. Approximately 2×10^7 cells were seeded and stimulated by 10 ng/mL IFN-β for 6 hours. Approximately more than 50 μg of total RNA was subjected to isolate poly (A) mRNA with poly-T oligo attached magnetic beads (cat. #61006,

Invitrogen). Following purification, the poly(A) mRNA fractions is fragmented into ~100-nt-long oligonucleotides using divalent cations under elevated temperature. Then the cleaved RNA fragments were subjected to incubation for 2h at 4°C with m^6A-specific antibody (cat. #202003, Synaptic Systems) in IP buffer (50 mM Tris-HCl, 750 mM NaCl and 0.5% Igepal CA-630) supplemented with BSA (0.5 μg/μL). The mixture was then incubated with protein-A beads and eluted with elution buffer (1×IP buffer and 6.7mM m^6A), while 10% of fragmented mRNA was kept as input. After immunoprecipitation, precipitates were washed by IP buffer for 5 times and RNA was isolated by adding TRIzol reagent. Purified m^6A-containing mRNA fragments and untreated mRNA input control fragments are converted to final cDNA library in accordance with a strand-specific library preparation by dUTP method, and analyzed by qPCR assay. The primers used in qPCR were listed in *Supplementary Appendix, Table S2*.

For MeRIP-Seq, approximately 5×10^7 cells were seeded and stimulated by 10 ng/mL IFN-β for 4 hours. After stimulation, total RNA was extracted using TRIzol reagent. The total RNA quality and quantity were analysis of Bioanalyzer 2100 and RNA 6000 Nano LabChip Kit (Agilent, CA, USA) with RIN number >7.0, followed with MeRIP assay. And then we performed the paired-end 2×150 bp sequencing on an Illumina Novaseq 6000 platform at the LC-BIO Bio-tech ltd (Hangzhou, China) following the vendor's recommended protocol. Details of MeRIP-Seq data analysis were shown in *Supplementary Appendix, Extended Methods*.

Immunofluorescence staining (IF) and imaging.

THP-1-derived macrophages were differentiated and stimulated as described above. After stimulation, cells were fixed by in 4% paraformaldehyde (Meilunbio, China) for 15 minutes at room temperature, permeated by ice-cold methanol at -20 °C for 15 minutes and blocked using 6% goat serum (cat. #AR1009, Boster Biological) for 1 hour, and then incubated with indicated primary antibody at 4°C overnight, followed by incubation with indicated secondary antibody at room temperature for 1 hour. Phosphate buffer (PBS) was used to wash three times for 5 minutes between each

step. After staining, Leica TCS-SP8 STED 3X confocal fluorescence microscope was used to acquire images. Images were captured by Leica TCS-SP8 STED 3X confocal fluorescence microscope and analyzed by Leica Application Suite Advanced Fluorescence (LAS AF, Version 4.2) software, while deconvolution was conducted by Huygens Software (Version 23.04). The colocalization between proteins was quantified by ImageJ software (National Institutes of Health, Maryland, USA, Version 1.52) using Pearson's correlation coefficient, ranging from -1 to 1. A value of -1 represents perfect negative correlation, 0 means no correlation and 1 indicates perfect correlation.

Expression, purification, and interaction of mCherry-WT WTAP, 5ST-A/ST-D mutants, CFP-METTL3 and GFP-STAT1.

Procedures of the expression of proteins in *E.* coli were referred to Hao Jiang et al(Jiang et al., 2015). Recombinant mCherry-WTAP, CFP-METTL3 and GFP-STAT1 were cloned into pET-28A plasmid, while ST-D and 5ST-A mutants of WTAP were constructed by mutating the pET-28A-mCherry-WTAP plasmid using Muta-direct^{TM} Kit (Sbsgene, cat. #SDM-15). After transformed into *E.* coli, protein was extracted as shown in *Supplementary Appendix, Extended Methods*.

For detection of interaction among mCherry-WTAP or its indicated mutants, CFP-METTL3 and GFP-STAT, purified proteins were mixed using physiological buffer (20 mM Tris-HCl, pH 7.5, 150 mM KCl, 10% PEG8000) in the final concentration of 10 μM and placed on the slides. Mixtures were incubated and imaged at 37°C in a live-cell-imaging chamber of Leica TCS-SP8 STED 3X confocal fluorescence microscope while images were analyzed by LAS AF software.

Phase separation assay and fluorescence recovery after photobleaching (FRAP).

Expression, purification, and interaction of mCherry-WT WTAP, 5ST-A/ST-D mutants, CFP-METTL3 and GFP-STAT1 were shown in *Supplementary Appendix, Extended Methods*. For *in vitro* phase separation assay, recombinant mCherry-WT WTAP, NTD, CTD, ΔPLD, 5ST-D and 5ST-A mutants in indicated concentration were

mixed with physiological buffer (20 mM Tris-HCl, pH 7.5, 150 mM KCl, 10% PEG8000). After incubation, turbid solution in the 200 μL PCR tubes were directed observed. For further capture of fluorescence images, solution of recombinant mCherry-WTAP and physiological buffer were treated with or without hex at a final concentration of 10% and placed on dishes. Leica TCS-SP8 STED 3X confocal fluorescence microscope with live-cell-imaging chamber at 37°C was used to capture fluorescence images and the 3D images. For in cells separation assay, plasmids expression mCherry-WT WTAP, 5ST-D and 5ST-A were transfected into HeLa cells for 24 hours, and treated with or without 5% hex and 20 μg/mL digitonin for 1 hour. Leica TCS-SP8 STED 3X confocal fluorescence microscope with live-cell-imaging chamber at 37°C was used to capture fluorescence images. For observing the fusion of condensates, recombinant mCherry-WTAP mixed with physiological buffer or HeLa cells transfected with mCherry-WTAP plasmids were incubated in the live-cell-imaging chamber at 37°C and. Images were captured by Leica TCS-SP8 STED 3X confocal fluorescence microscope, while deconvolution was conducted by Huygens software.

For *in vitro* FRAP experiments were performed on Leica TCS-SP8 STED 3X confocal fluorescence microscope. Recombinant mCherry-WT WTAP, NTD, CTD, 5ST-D and 5ST-A mutants in indicated concentration was mixed with physiological buffer on dishes. For in cells FRAP experiment, HeLa cells transfected with mCherry-WT WTAP, 5ST-D and 5ST-A mutants were treated as indicated. Samples were imaged with Leica TCS-SP8 STED 3X confocal fluorescence microscope with live-cell-imaging chamber at 37°C. Spots of mCherry-WTAP foci were photobleached with 100% laser power using 567-nm lasers followed with time-lapse images. Images were analyzed by LAS AF software. Fluorescence intensities of regions of interest (ROIs) were corrected by unbleached control regions and then normalized to pre-bleached intensities of the ROIs.

Statistical Analysis.

The data of all quantitative experiments are represented as mean ± SEM of three independent experiments. Statistical analyses were performed with GraphPad Prism software version 8.0 (GraphPad software, California, USA) using one/two-way analysis of variance (ANOVA) followed by Tukey's test or unpaired two-tailed Student's *t*-test as described in the figure legends. P-value < 0.05 was considered as statistically significant of all statistical analyses.

Data availability.

Raw data of RNA-Seq and MeRIP-Seq have been deposited in the Sequence Read Archive (SRA) database under accession code PRJNA680033 and PRJNA680974, respectively. The data that support this study are available within the article and its Supplementary Information files or available from the authors upon request.

Acknowledgements This work was supported by the National Key R&D Program of China (2020YFA0908700), National Natural Science Foundation of China (82341047, 32270922, 31970700, 324B2026), and Guangdong Basic and Applied Basic Research Foundation (2020B1515120090).

Author Contributions: *J.C.* conceived the project. *J.C.*, *S.C.* and *J.Z.* designed the experiments. *S.C.*, *J.Z.* and *S.J.* expressed and purified the proteins using *E. coli* system while *S.C.*, *J.Z.* and C.Z. finished the rest of the experiments. *X.L.*, *J.R.*, *S.C.* and *J.Z.* analyzed the data of RNA-Seq and MeRIP-Seq. All authors discussed the results and commented on or prepared the manuscript.

Competing Interest: The authors declare no competing interests.

References

Alberti, S., Gladfelter, A., & Mittag, T. (2019). Considerations and Challenges in Studying Liquid-Liquid Phase Separation and Biomolecular Condensates. *Cell*, *176*(3), 419-434. doi:10.1016/j.cell.2018.12.035

Arendt, T., Stieler, J. T., & Holzer, M. (2016). Tau and tauopathies. *Brain Res Bull, 126*(Pt 3), 238-292. doi:10.1016/j.brainresbull.2016.08.018

Barbieri, I., Tzelepis, K., Pandolfini, L., Shi, J., Millan-Zambrano, G., Robson, S. C., . . . Kouzarides, T. (2017). Promoter-bound METTL3 maintains myeloid leukaemia by m(6)A-dependent translation control. *Nature, 552*(7683), 126-131. doi:10.1038/nature24678

Bertero, A., Brown, S., Madrigal, P., Osnato, A., Ortmann, D., Yiangou, L., . . . Vallier, L. (2018). The SMAD2/3 interactome reveals that TGFβ controls m6A mRNA methylation in pluripotency. *Nature, 555*(7695), 256-259. doi:10.1038/nature25784

Bhattarai, P. Y., Kim, G., Lim, S. C., & Choi, H. S. (2024). METTL3-STAT5B interaction facilitates the co-transcriptional m(6)A modification of mRNA to promote breast tumorigenesis. *Cancer Lett, 603*, 217215. doi:10.1016/j.canlet.2024.217215

Boyko, S., Qi, X., Chen, T. H., Surewicz, K., & Surewicz, W. K. (2019). Liquid-liquid phase separation of tau protein: The crucial role of electrostatic interactions. *J Biol Chem, 294*(29), 11054-11059. doi:10.1074/jbc.AC119.009198

Chen, Y., Peng, C., Chen, J., Chen, D., Yang, B., He, B., . . . Zheng, S. (2019). WTAP facilitates progression of hepatocellular carcinoma via m6A-HuR-dependent epigenetic silencing of ETS1. *Mol Cancer, 18*(1), 127. doi:10.1186/s12943-019-1053-8

Cui, J., Song, Y., Li, Y., Zhu, Q., Tan, P., Qin, Y., . . . Wang, R. F. (2014). USP3 inhibits type I interferon signaling by deubiquitinating RIG-I-like receptors. *Cell Res, 24*(4), 400-416. doi:10.1038/cr.2013.170

Dou, X., Xiao, Y., Shen, C., Wang, K., Wu, T., Liu, C., . . . He, C. (2023). RBFOX2 recognizes N(6)-methyladenosine to suppress transcription and block myeloid leukaemia differentiation. *Nat Cell Biol, 25*(9), 1359-1368. doi:10.1038/s41556-023-01213-w

Gabryelczyk, B., Cai, H., Shi, X., Sun, Y., Swinkels, P. J. M., Salentinig, S., . . . Miserez, A. (2019). Hydrogen bond guidance and aromatic stacking drive liquid-liquid phase separation of intrinsically disordered histidine-rich peptides. *Nat Commun, 10*(1), 5465. doi:10.1038/s41467-019-13469-8

Gao, Y., Pei, G., Li, D., Li, R., Shao, Y., Zhang, Q. C., & Li, P. (2019). Multivalent m^6A motifs promote phase separation of YTHDF proteins. *Cell Res, 29*(9), 767-769. doi:10.1038/s41422-019-0210-3

Garcias Morales, D., & Reyes, J. L. (2021). A birds'-eye view of the activity and specificity of the mRNA m^6A methyltransferase complex. *Wiley Interdiscip Rev RNA, 12*(1), e1618. doi:10.1002/wrna.1618

Ge, Y., Ling, T., Wang, Y., Jia, X., Xie, X., Chen, R., . . . Xu, A. (2021). Degradation of WTAP blocks antiviral responses by reducing the m^6A levels of IRF3 and IFNAR1 mRNA. *EMBO Rep, 22*(11), e52101. doi:10.15252/embr.202052101

Geula, S., Moshitch-Moshkovitz, S., Dominissini, D., Mansour, A. A., Kol, N., Salmon-Divon, M., . . . Hanna, J. H. (2015). Stem cells. m6A mRNA methylation facilitates resolution of naive pluripotency toward differentiation. *Science, 347*(6225), 1002-1006. doi:10.1126/science.1261417

Goubau, D., Deddouche, S., & Reis e Sousa, C. (2013). Cytosolic sensing of viruses. *Immunity, 38*(5), 855-869. doi:10.1016/j.immuni.2013.05.007

Gourfinkel-An, I., Cancel, G., Trottier, Y., Devys, D., Tora, L., Lutz, Y., . . . Hirsch, E. C. (1997). Differential distribution of the normal and mutated forms of huntingtin in the human brain. *Ann Neurol, 42*(5), 712-719. doi:10.1002/ana.410420507

Guccione, E., & Richard, S. (2019). The regulation, functions and clinical relevance of arginine methylation. *Nat Rev Mol Cell Biol, 20*(10), 642-657. doi:10.1038/s41580-019-0155-x

Han, D., Longhini, A. P., Zhang, X., Hoang, V., Wilson, M. Z., & Kosik, K. S. (2022). Dynamic assembly of the mRNA m6A methyltransferase complex is regulated by METTL3 phase separation. *PLoS Biol, 20*(2), e3001535. doi:10.1371/journal.pbio.3001535

He, P. C., Wei, J., Dou, X., Harada, B. T., Zhang, Z., Ge, R., . . . He, C. (2023). Exon architecture controls mRNA m(6)A suppression and gene expression. *Science, 379*(6633), 677-682. doi:10.1126/science.abj9090

Henault, J., Riggs, J. M., Karnell, J. L., Liarski, V. M., Li, J., Shirinian, L., . . . Sanjuan, M. A. (2016). Self-reactive IgE exacerbates interferon responses associated with autoimmunity. *Nat Immunol, 17*(2), 196-203. doi:10.1038/ni.3326

Hou, S., Hu, J., Yu, Z., Li, D., Liu, C., & Zhang, Y. (2024). Machine learning predictor PSPire screens for phase-separating proteins lacking intrinsically disordered regions. *Nat Commun, 15*(1), 2147. doi:10.1038/s41467-024-46445-y

Hu, H., Miao, Y. R., Jia, L. H., Yu, Q. Y., Zhang, Q., & Guo, A. Y. (2019). AnimalTFDB 3.0: a comprehensive resource for annotation and prediction of animal transcription factors. *Nucleic Acids Res, 47*(D1), D33-D38. doi:10.1093/nar/gky822

Huang, H., Weng, H., Zhou, K., Wu, T., Zhao, B. S., Sun, M., . . . Chen, J. (2019). Histone H3 trimethylation at lysine 36 guides m(6)A RNA modification co-transcriptionally. *Nature, 567*(7748), 414-419. doi:10.1038/s41586-019-1016-7

Huang, Q., Mo, J., Liao, Z., Chen, X., & Zhang, B. (2022). The RNA m^6A writer WTAP in diseases: structure, roles, and mechanisms. *Cell Death Dis, 13*(10), 852. doi:10.1038/s41419-022-05268-9

Jia, G., Fu, Y., Zhao, X., Dai, Q., Zheng, G., Yang, Y., . . . He, C. (2011). N6-Methyladenosine in nuclear RNA is a major substrate of the obesity-associated FTO. *Nature Chemical Biology, 7*(12), 885-887. doi:10.1038/nchembio.687

Jiang, H., Wang, S., Huang, Y., He, X., Cui, H., Zhu, X., & Zheng, Y. (2015). Phase transition of spindle-associated protein regulate spindle apparatus assembly. *Cell, 163*(1), 108-122. doi:10.1016/j.cell.2015.08.010

Keene, J. D., Komisarow, J. M., & Friedersdorf, M. B. (2006). RIP-Chip: the isolation and identification of mRNAs, microRNAs and protein components of

ribonucleoprotein complexes from cell extracts. *Nat Protoc, 1*(1), 302-307. doi:10.1038/nprot.2006.47

Knuckles, P., & Bühler, M. (2018). Adenosine methylation as a molecular imprint defining the fate of RNA. *FEBS Letters, 592*(17), 2845-2859. doi:10.1002/1873-3468.13107

Lee, J. H., Wang, R., Xiong, F., Krakowiak, J., Liao, Z., Nguyen, P. T., . . . Li, W. (2021). Enhancer RNA m6A methylation facilitates transcriptional condensate formation and gene activation. *Mol Cell, 81*(16), 3368-3385 e3369. doi:10.1016/j.molcel.2021.07.024

Li, J., Chen, K., Dong, X., Xu, Y., Sun, Q., Wang, H., . . . Luo, M. (2022). YTHDF1 promotes mRNA degradation via YTHDF1-AGO2 interaction and phase separation. *Cell Prolif, 55*(1), e13157. doi:10.1111/cpr.13157

Li, Z. X., Zheng, Z. Q., Yang, P. Y., Lin, L., Zhou, G. Q., Lv, J. W., . . . Sun, Y. (2022). WTAP-mediated m^6A modification of lncRNA DIAPH1-AS1 enhances its stability to facilitate nasopharyngeal carcinoma growth and metastasis. *Cell Death Differ, 29*(6), 1137-1151. doi:10.1038/s41418-021-00905-w

Luo, Y. Y., Wu, J. J., & Li, Y. M. (2021). Regulation of liquid-liquid phase separation with focus on post-translational modifications. *Chem Commun (Camb), 57*(98), 13275-13287. doi:10.1039/d1cc05266g

Luo, Z., Ma, Q., Sun, S., Li, N., Wang, H., Ying, Z., & Ke, S. (2023). Exon-intron boundary inhibits m(6)A deposition, enabling m(6)A distribution hallmark, longer mRNA half-life and flexible protein coding. *Nat Commun, 14*(1), 4172. doi:10.1038/s41467-023-39897-1

Markevich, N. I., Hoek, J. B., & Kholodenko, B. N. (2004). Signaling switches and bistability arising from multisite phosphorylation in protein kinase cascades. *J Cell Biol, 164*(3), 353-359. doi:10.1083/jcb.200308060

McFadden, M. J., McIntyre, A. B. R., Mourelatos, H., Abell, N. S., Gokhale, N. S., Ipas, H., . . . Horner, S. M. (2021). Post-transcriptional regulation of antiviral

gene expression by N6-methyladenosine. *Cell Rep, 34*(9), 108798. doi:10.1016/j.celrep.2021.108798

McFadden, M. J., Sacco, M. T., Murphy, K. A., Park, M., Gokhale, N. S., Somfleth, K. Y., & Horner, S. M. (2022). FTO Suppresses STAT3 Activation and Modulates Proinflammatory Interferon-Stimulated Gene Expression. *J Mol Biol, 434*(6), 167247. doi:10.1016/j.jmb.2021.167247

Meyer, K. D., & Jaffrey, S. R. (2017). Rethinking m^6A Readers, Writers, and Erasers. *Annu Rev Cell Dev Biol, 33*, 319-342. doi:10.1146/annurev-cellbio-100616-060758

Mowen, K. A., Tang, J., Zhu, W., Schurter, B. T., Shuai, K., Herschman, H. R., & David, M. (2001). Arginine methylation of STAT1 modulates IFNalpha/beta-induced transcription. *Cell, 104*(5), 731-741. doi:10.1016/s0092-8674(01)00269-0

Murthy, A. C., Dignon, G. L., Kan, Y., Zerze, G. H., Parekh, S. H., Mittal, J., & Fawzi, N. L. (2019). Molecular interactions underlying liquid-liquid phase separation of the FUS low-complexity domain. *Nat Struct Mol Biol, 26*(7), 637-648. doi:10.1038/s41594-019-0250-x

Oerum, S., Meynier, V., Catala, M., & Tisne, C. (2021). A comprehensive review of m6A/m6Am RNA methyltransferase structures. *Nucleic Acids Res, 49*(13), 7239-7255. doi:10.1093/nar/gkab378

Perutz, M. F. (1996). Glutamine repeats and inherited neurodegenerative diseases: molecular aspects. *Curr Opin Struct Biol, 6*(6), 848-858. doi:10.1016/s0959-440x(96)80016-9

Qin, Y., Liu, Q., Tian, S., Xie, W., Cui, J., & Wang, R. F. (2016). TRIM9 short isoform preferentially promotes DNA and RNA virus-induced production of type I interferon by recruiting GSK3beta to TBK1. *Cell Res, 26*(5), 613-628. doi:10.1038/cr.2016.27

Reichheld, S. E., Muiznieks, L. D., Keeley, F. W., & Sharpe, S. (2017). Direct observation of structure and dynamics during phase separation of an

elastomeric protein. *Proc Natl Acad Sci U S A, 114*(22), E4408-E4415. doi:10.1073/pnas.1701877114

Ries, R. J., Zaccara, S., Klein, P., Olarerin-George, A., Namkoong, S., Pickering, B. F., . . . Jaffrey, S. R. (2019). m^6A enhances the phase separation potential of mRNA. *Nature, 571*(7765), 424-428. doi:10.1038/s41586-019-1374-1

Rubio, R. M., Depledge, D. P., Bianco, C., Thompson, L., & Mohr, I. (2018). RNA m^6A modification enzymes shape innate responses to DNA by regulating interferon beta. *Genes Dev, 32*(23-24), 1472-1484. doi:10.1101/gad.319475.118

Schapira, M. (2016). Structural Chemistry of Human RNA Methyltransferases. *ACS Chem Biol, 11*(3), 575-582. doi:10.1021/acschembio.5b00781

Schneider, W. M., Chevillotte, M. D., & Rice, C. M. (2014). Interferon-stimulated genes: a complex web of host defenses. *Annu Rev Immunol, 32*, 513-545. doi:10.1146/annurev-immunol-032713-120231

Sendinc, E., & Shi, Y. (2023). RNA m6A methylation across the transcriptome. *Mol Cell, 83*(3), 428-441. doi:10.1016/j.molcel.2023.01.006

Shi, H., Wang, X., Lu, Z., Zhao, B. S., Ma, H., Hsu, P. J., . . . He, C. (2017). YTHDF3 facilitates translation and decay of N(6)-methyladenosine-modified RNA. *Cell Res, 27*(3), 315-328. doi:10.1038/cr.2017.15

Tanaka, M., Morishima, I., Akagi, T., Hashikawa, T., & Nukina, N. (2001). Intra- and intermolecular beta-pleated sheet formation in glutamine-repeat inserted myoglobin as a model for polyglutamine diseases. *J Biol Chem, 276*(48), 45470-45475. doi:10.1074/jbc.M107502200

Uddin, S., Sassano, A., Deb, D. K., Verma, A., Majchrzak, B., Rahman, A., . . . Platanias, L. C. (2002). Protein kinase C-delta (PKC-delta) is activated by type I interferons and mediates phosphorylation of Stat1 on serine 727. *Journal Of Biological Chemistry, 277*(17), 14408-14416. doi:10.1074/jbc.M109671200

Uzonyi, A., Dierks, D., Nir, R., Kwon, O. S., Toth, U., Barbosa, I., . . . Schwartz, S. (2023). Exclusion of m6A from splice-site proximal regions by the exon

junction complex dictates m6A topologies and mRNA stability. *Mol Cell, 83*(2), 237-251 e237. doi:10.1016/j.molcel.2022.12.026

Wang, A., Tao, W., Tong, J., Gao, J., Wang, J., Hou, G., . . . Zhu, S. (2022). m6A modifications regulate intestinal immunity and rotavirus infection. *Elife, 11*. doi:10.7554/eLife.73628

Wang, J., Choi, J.-M., Holehouse, A. S., Lee, H. O., Zhang, X., Jahnel, M., . . . Hyman, A. A. (2018). A Molecular Grammar Governing the Driving Forces for Phase Separation of Prion-like RNA Binding Proteins. *Cell, 174*(3), 688-699.e616. doi:10.1016/j.cell.2018.06.006

Wang, J., Wang, L., Diao, J., Shi, Y. G., Shi, Y., Ma, H., & Shen, H. (2020). Binding to m^6A RNA promotes YTHDF2-mediated phase separation. *Protein Cell, 11*(4), 304-307. doi:10.1007/s13238-019-00660-2

Wang, L., Hui, H., Agrawal, K., Kang, Y., Li, N., Tang, R., . . . Rana, T. M. (2020). m^6A RNA methyltransferases METTL3/14 regulate immune responses to anti-PD-1 therapy. *EMBO J, 39*(20), e104514. doi:10.15252/embj.2020104514

Wang, L., Wen, M., & Cao, X. (2019). Nuclear hnRNPA2B1 initiates and amplifies the innate immune response to DNA viruses. *Science, 365*(6454). doi:10.1126/science.aav0758

Wang, X., Lu, Z., Gomez, A., Hon, G. C., Yue, Y., Han, D., . . . He, C. (2014). N6-methyladenosine-dependent regulation of messenger RNA stability. *Nature, 505*(7481), 117-120. doi:10.1038/nature12730

Wang, X., Zhao, B. S., Roundtree, I. A., Lu, Z., Han, D., Ma, H., . . . He, C. (2015). N(6)-methyladenosine Modulates Messenger RNA Translation Efficiency. *Cell, 161*(6), 1388-1399. doi:10.1016/j.cell.2015.05.014

Wen Z, Zhong Z, & Jr., D. J. (1995). Maximal activation of transcription by Stat1 and Stat3 requires both tyrosine and serine phosphorylation. *Cell, 82*(2), 241-250. doi:10.1016/0092-8674(95)90311-9

Winkler, R., Gillis, E., Lasman, L., Safra, M., Geula, S., Soyris, C., . . . Stern-Ginossar, N. (2019). m^6A modification controls the innate immune response to

infection by targeting type I interferons. *Nat Immunol, 20*(2), 173-182. doi:10.1038/s41590-018-0275-z

Xu, W., He, C., Kaye, E. G., Li, J., Mu, M., Nelson, G. M., . . . Shen, H. (2022). Dynamic control of chromatin-associated m(6)A methylation regulates nascent RNA synthesis. *Mol Cell, 82*(6), 1156-1168 e1157. doi:10.1016/j.molcel.2022.02.006

Yang, X., Triboulet, R., Liu, Q., Sendinc, E., & Gregory, R. I. (2022). Exon junction complex shapes the m(6)A epitranscriptome. *Nat Commun, 13*(1), 7904. doi:10.1038/s41467-022-35643-1

Yu, H., Zhao, K., Zeng, H., Li, Z., Chen, K., Zhang, Z., . . . Wu, Z. (2021). N^6-methyladenosine (m^6A) methyltransferase WTAP accelerates the Warburg effect of gastric cancer through regulating HK2 stability. *Biomed Pharmacother, 133*, 111075. doi:10.1016/j.biopha.2020.111075

Zhang, H., Shao, S., Zeng, Y., Wang, X., Qin, Y., Ren, Q., . . . Sun, Y. (2022). Reversible phase separation of HSF1 is required for an acute transcriptional response during heat shock. *Nat Cell Biol, 24*(3), 340-352. doi:10.1038/s41556-022-00846-7

Zhang, Z., Theler, D., Kaminska, K. H., Hiller, M., de la Grange, P., Pudimat, R., . . . Stamm, S. (2010). The YTH domain is a novel RNA binding domain. *J Biol Chem, 285*(19), 14701-14710. doi:10.1074/jbc.M110.104711

Zheng, G., Dahl, J. A., Niu, Y., Fedorcsak, P., Huang, C. M., Li, C. J., . . . He, C. (2013). ALKBH5 is a mammalian RNA demethylase that impacts RNA metabolism and mouse fertility. *Mol Cell, 49*(1), 18-29. doi:10.1016/j.molcel.2012.10.015

Zhong, X., Yu, J., Frazier, K., Weng, X., Li, Y., Cham, C. M., . . . Leone, V. (2018). Circadian Clock Regulation of Hepatic Lipid Metabolism by Modulation of m^6A mRNA Methylation. *Cell Rep, 25*(7), 1816-1828 e1814. doi:10.1016/j.celrep.2018.10.068

Figure legends

Figure 1 WTAP goes through phase transition with IFN-β stimulation.

(A) THP-1-derived macrophages were infected with Vesicular Stomatitis Virus (VSV) (m.o.i. = 0.1) for 24 hours together with or without 5% 1,6-hexanediol (hex) and 10 μg/mL digitonin for 2 hours or left untreated (UT). Endogenous WTAP was stained and imaged using confocal microscopy. The number of WTAP condensates that diameter over 0.4 μm of n = 20 cells were counted through ImageJ and shown. Scale bars indicated 5 μm.

(B) HeLa cells were placed on the dishes and stimulated with or without 10 ng/mL IFN-β for 1 hour at 37 °C. Endogenous WTAP was stained and imaged using confocal microscopy. The number of WTAP condensates that diameter over 0.4 μm of n = 80 cells were counted through ImageJ and shown. Scale bars indicated 5 μm.

(C) Domain structures (top) and distribution of amino acids (bottom) of WTAP protein. WT, wild type. NTD, N-terminal domain. CTD, C-terminal domain. NLS, nuclear localization signal. IDR, intrinsically disordered regions. Gln, Glutamine. Ser, Serine. Lue, Leucine. Glu, Glutamic acid.

(D) Tubes containing physiological buffer with recombinant mCherry (10 μM) or mCherry-WTAP (10 μM) were compared, in which recombinant mCherry-WTAP underwent phase separation.

(E) Foci formation of recombinant mCherry-WTAP (10 μM) with or without 5% 1,6-hexanediol (hex) *in vitro* was observed through confocal microscopy. Scale bars indicated 5 μm.

(F) Phase separation of mCherry-WTAP in mCherry-WTAP-rescued HeLa cells treated with or without 5% hex and 20 μg/mL digitonin were observed through confocal microscopy. Representative images of n = 20 cells were shown. Scale bars indicated 5 μm.

(G) mCherry-WTAP-rescued HeLa cells were placed on dishes and treated with or without 10 ng/mL IFN-β for 1 hour at 37 °C. After stimulation, bleaching of the WTAP foci was performed and quantification of fluorescence recovery after photobleaching (FRAP) of mCherry-WTAP aggregates was analyzed. The start time

point of recovery after photobleaching was defined as 0 second. Representative images of n = 10 cells were shown. Scale bars indicated 5 μm.

(H) Recombinant mCherry-WT WTAP, NTD and CTD (10 μM) were mixed with the physiological buffer and placed on the dishes at 37°C (Prebleach). After incubation, bleaching was performed and quantification of FRAP of recombinant mCherry-WT WTAP, NTD and CTD were analyzed. Representative images of n = 6 condensates were shown, and the normalized intensity was measured and analyzed. The start time point of recovery after photobleaching was defined as 0 second. Scale bars indicated 2 μm.

All error bars, mean values ± SD, P-values were determined by unpaired two-tailed Student's *t*-test of n = 20 cells in (A) and n = 80 cells in (B). For (A-B and D-H), similar results were obtained for three independent biological experiments.

Figure 2. IFN-β-mediated dephosphorylation of WTAP induces its phase transition.

(A) THP-1-derived macrophages were treated with 10 ng/mL IFN-β for 1 hour or left untreated. Whole cell lysate (WCL) was collected and immunoprecipitation (IP) experiment using anti-WTAP antibody or rabbit IgG was performed, followed with immunoblot. pWTAP was detected by anti-phosphoserine/threonine/tyrosine antibody (pan-p). Relative protein level was shown.

(B) THP-1-derived macrophages were treated with 10 ng/mL IFN-β for 1 hour or left untreated. WCL was collected and IP experiment using anti-WTAP antibody or rabbit IgG was performed, followed with immunoblot.

(C) THP-1-derived macrophages were transfected with *scramble* (*scr*) or *PPP4*-targeted siRNA and stimulated with or without 10 ng/mL IFN-β for 1 hour. WCL was collected and IP experiment with anti-WTAP antibody or rabbit IgG was performed, followed with immunoblot. pWTAP was detected by anti-phosphoserine/threonine/tyrosine antibody (pan-p). Relative protein level was measured and analyzed.

(D) mCherry-WTAP was purified from HEK 293T cells expressing mCherry-WTAP using anti-WTAP antibody and analyzed by mass spectrometry (MS) for the phosphorylation. Six phosphorylated residues were identified. Data of MS assay for five phosphorylated sites within CTD were shown in Figure 2-figure supplement 1D.

(E-F) Recombinant mCherry-WTAP mutants with indicated serine/threonine (S/T) to aspartic acid (D) or alanine (A) mutation were listed in (E), while representative images of the phase-separated mCherry-WT WTAP, 5ST-D and 5ST-A mutants were shown in (F). Images of phase separation of other mCherry-WTAP mutants (10 μM) were shown in Figure 2-figure supplement 1E. Scale bars indicated 5 μm.

(G) Recombinant mCherry-WT WTAP (10 μM), 5ST-D mutant (10 μM) or 5ST-A mutant (10 μM) was mixed with the physiological buffer and placed on the dishes at 37°C (Prebleach). After incubation, bleaching was performed and quantification of fluorescence recovery after photobleaching (FRAP) of recombinant mCherry-WT WTAP, 5ST-D or 5ST-A mutant were analyzed. Representative images of n = 5 condensates were shown and the normalized intensity was measured and analyzed. The start time point of recovery after photobleaching was defined as 0 second. Arrow indicated the FRAP area while scale bars indicated 2 μm.

(H) mCherry-WT WTAP, 5ST-D or 5ST-A mutants-rescued HeLa cells were placed on the dishes and stimulated with or without 10 ng/mL IFN-β for 1 hour at 37°C. After seeding, bleaching of the WTAP foci was performed and quantification of FRAP of mCherry-WTAP aggregates was analyzed. Representative images of n = 10 cells were shown, and the normalized intensity was measured and analyzed. The start time point of recovery after photobleaching was defined as 0 second. Scale bars indicated 5 μm.

(I) Schematic figure of phase separation of WT WTAP, 5ST-D and 5ST-A *in vitro* (above) and WT WTAP with IFN-β stimulation or left untreated (UT), 5ST-D and 5ST-A in cells (below).

All error bars, mean values ± SD, P-values were determined by unpaired two-tailed Student's *t*-test of n = 3 independent biological experiments in (A and C). For (A-C and E-H), similar results were obtained for three independent biological experiments.

Figure 3. WTAP is crucial for the m^{6}A modification and expression of ISG mRNAs.

(A) Transcriptome sequencing analysis of control (*GFP*^{sgRNA}) and *WTAP*^{sgRNA} #2 THP-1-derived macrophages stimulated with 10 ng/mL IFN-β for 0, 6, 12 hours. The count-per-million (CPM) value of the ISGs was drawn by Heatmapper and clustered using Centroid Linkage approach.

(B) Volcano plots showing the changes in transcripts level of IFN-β up-regulated genes in *WTAP*^{sgRNA} THP-1-derived macrophages versus control (*GFP*^{sgRNA}) cells under IFN-β stimulation for 6 and 12 hours. Red dots indicated the significantly up-regulated genes in *WTAP*^{sgRNA} cells ($\log_2$(fold change) > 1 while adjusted P-value (p_{adj}) < 0.05).

(C) Gene ontology analysis for the WTAP down-regulated ISGs.

(D) TPMs showing the changes in transcripts level of *IFIT1*, *IFIT2*, *OAS1* and *OAS2* in control (*GFP*^{sgRNA}) and *WTAP*^{sgRNA} #2 THP-1-derived macrophages stimulated with 10 ng/mL IFN-β for 6 or 12 hours or left untreated.

(E-F) Control (*GFP*^{sgRNA}) and *WTAP*^{sgRNA} #2 THP-1-derived macrophages were treated with 10 ng/mL IFN-β for 4 hours, m^{6}A modification analyzed by m^{6}A methylated RNA immunoprecipitation (IP) followed by deep sequencing (MeRIP-seq). Distribution (E) and topology (F) analysis (5'-untranslated regions (UTR), coding sequences (CDS) and 3'-UTR) of total m^{6}A sites in control (*GFP*^{sgRNA}) cells or WTAP-dependent m^{6}A sites.

(G) Percentage of m^{6}A-modified ISGs including core ISGs or WTAP down-regulated ISGs were calculated and presented.

(H) Topology analysis (5'-UTR, CDS and 3'-UTR) of ISGs m^{6}A sites and non-ISGs m^{6}A sites.

(I) Control (*GFP*^{sgRNA}) and *WTAP*^{sgRNA} #2 THP-1-derived macrophages were treated with 10 ng/mL IFN-β for 4 hours. MeRIP-quantitative real time-polymerase chain reaction (qPCR) assay of *IFIT1*, *IFIT2*, *OAS1* and *OAS2* was performed and ratios between m^{6}A-modified mRNA and input were shown (m^{6}A IP/input).

(J) Control (*GFP*^{sgRNA}), *WTAP*^{sgRNA} #1 and *WTAP*^{sgRNA} #2 THP-1-derived macrophages were treated with 10 ng/mL IFN-β for 2 hours. After IFN-β treatment, medium with stimuli was replaced by 5 μM actinomycin D (Act D) for indicated time points. RNA was collected and detected by qPCR assay.

(K) Control (*GFP*^{sgRNA}), *WTAP*^{sgRNA} #1 and *WTAP*^{sgRNA} #2 THP-1-derived macrophages were treated with 10 ng/mL IFN-β for indicated time points. Expression of *IFIT1*, *IFIT2*, *OAS1* and *OAS2* mRNA was analyzed through qPCR assays.

All error bars, mean values ± SEM, P-values were determined by unpaired two-tailed Student's *t*-test of n = 3 independent biological experiments in (I). All error bars, mean values ± SEM, P-values were determined by two-way ANOVA test of n = 3 independent biological experiments in (J-K).

Figure 4. Liquid-phase separation of WTAP mediates m^{6}A modification and ISGs expression.

(A) Control (*GFP*^{sgRNA}) and *WTAP*^{sgRNA} #2 THP-1-derived macrophages were treated with 10 ng/mL IFN-β together with or without 5% 1,6-hexanediol (hex) and 20 μg/mL digitonin for 4 hours or left untreated. MeRIP-qPCR analysis of *IFIT1*, *IFIT2*, *OAS1* and *OAS2* was performed and ratios between m^{6}A-modified mRNA and input were shown (m^{6}A IP/input).

(B) THP-1-derived macrophages transfected with *scramble* (*scr)* siRNA or *PPP4* siRNA were treated with 10 ng/mL IFN-β for 4 hours. MeRIP-qPCR assay of *IFIT1*, *IFIT2*, *OAS1* and *OAS2* was performed and ratios between m^{6}A-modified mRNA and input were shown (m^{6}A IP/input).

(C) THP-1-derived macrophages were pre-treated with 2 nM or 5 nM fostriecin for 24 hours or left untreated, followed with 10 ng/mL IFN-β for 4 hours. MeRIP-qPCR analysis of *IFIT1*, *IFIT2*, *OAS1* and *OAS2* was performed and ratios between m^{6}A-modified mRNA and input were shown (m^{6}A IP/input).

(D) Control (*GFP*^{sgRNA}) and *WTAP*^{sgRNA} #2 THP-1-derived macrophages with or without expression of Flag-tagged wild type (WT) WTAP, and its 5ST-D or 5ST-A mutants were treated with 10 ng/mL IFN-β for 4 hours. MeRIP-qPCR assay of *IFIT1*,

IFIT2, *OAS1* and *OAS2* was performed and ratios between m^6A-modified mRNA and input were shown (m^6A IP/input).

(E) Wild type (WT) WTAP, 5ST-D or 5ST-A mutant-rescued *WTAP*^{sgRNA} THP-1-derived macrophages were treated with 10 ng/mL IFN-β for 4 hours. MeRIP-qPCR assay of *IFIT1*, *IFIT2*, *OAS1* and *OAS2* was performed and ratios between m^6A-modified mRNA and input were shown (m^6A IP/input).

All error bars, mean values ± SEM, P-values were determined by two-way ANOVA test of n = 3 independent biological experiments in (A, E). All error bars, mean values ± SEM, P-values were determined by unpaired two-tailed Student's *t*-test of n = 3 independent biological experiments in (B-C). All error bars, mean values ± SEM, P-values were determined by one-way ANOVA test of n = 3 independent biological experiments in (D).

Figure 5. Liquid-phase separated WTAP bridges STAT1 and m^6A modification methyltransferase complex to direct m^6A modification on ISG mRNAs.

(A) Occupancy of the promoter of the WTAP down-regulated ISGs with lower m^6A level in *WTAP*^{sgRNA} #2 cells (genes were identified in Figure 3A and both -2000-0 bp and -500-0 bp upstream of transcription start site were analyzed) by STAT1, STAT2 and IRF9 was predicted by AnimalTFDB 3.0.

(B) THP-1-derived macrophages were treated with 10 ng/mL IFN-β for indicated time points. Whole cell lysate (WCL) was collected and immunoprecipitation (IP) experiment using anti-STAT1 antibody or rabbit IgG was performed, followed with immunoblot.

(C) Control (*GFP*^{sgRNA}) and *WTAP*^{sgRNA} #2 THP-1-derived macrophages were treated with 10 ng/mL IFN-β for 1 hour or left untreated. WCL was collected and IP experiment using anti-METTL3 antibody or rabbit IgG was performed, followed with immunoblot.

(D) Control (*GFP*^{sgRNA}) and *WTAP*^{sgRNA} #2 THP-1-derived macrophages were treated with 10 ng/mL IFN-β for 2 hour or left untreated. RNA immunoprecipitation (RIP) experiments using anti-METTL3 antibody or rabbit IgG control were performed in

control and *WTAP*^{sgRNA} #2 THP-1-derived macrophages treated with 10 ng/mL IFN-β for 2 hours. RNA of ISGs enriched by RIP was analyzed by quantitative real time-polymerase chain reaction (qPCR) assay, and the ratios between RIP-enriched RNA and input were shown (RIP enrichment/input).

(E) THP-1-derived macrophages were treated with 10 ng/mL IFN-β for indicated time points together with or without 5% 1,6-hexanediol (hex) and 20 μg/mL digitonin. WCL was collected and IP experiment with anti-STAT1 antibody or rabbit IgG was performed, followed with immunoblot.

(F) Recombinant GFP-STAT1 (10 μM) and mCherry-WTAP (10 μM) were incubated with or without 5% hex *in vitro*. IP experiment with anti-STAT1 antibody or rabbit IgG was performed, followed with immunoblot.

(G) THP-1-derived macrophages were treated with 10 ng/mL IFN-β only or with 5% hex and 20 μg/mL digitonin for 1 hour or left untreated (UT). Interaction between STAT1 (green) and WTAP (red) were imaged using confocal microscope. Pearson's correlation coefficient was analyzed and calculated from n = 80 cells through ImageJ. Scale bars indicated 5 μm.

(H-I) Recombinant GFP-STAT1 (10 μM), mCherry-WTAP (10 μM) and CFP-METTL3 (10 μM) were incubated using physiological buffer at 37°C *in vitro*. After incubation, images were captured using confocal microscope (H). Relative fluorescence intensity of proteins in n = 10 condensates were analyzed by ImageJ software (I).

All error bars, mean values ± SEM, P-values were determined by unpaired two-tailed Student's *t*-test of n = 3 independent biological experiments in (D). All error bars, mean values ± SD, P-values were determined by unpaired two-tailed Student's *t*-test of n = 80 cells in (G) and n = 3 independent biological experiments in (I). For (B-D, E-G and H), similar results were obtained for three independent biological experiments.

Figure 6. Phase transition of WTAP mediates its interaction with ISGs promoter regions to regulate m^{6}A modification on ISG mRNAs.

(A) Chromatin immunoprecipitation (ChIP) experiments using anti-STAT1 antibody or rabbit IgG control were performed in THP-1-derived macrophages treated with 10 ng/mL IFN-β for 2 hours or left untreated. Binding between the promoter regions of *IFIT1*, *IFIT2*, *OAS1* and *OAS2* with WTAP was detected by quantitative real time-polymerase chain reaction (qPCR) assay. Ratios between ChIP-enriched DNA and input were shown (ChIP enrichment/input).

(B) ChIP experiments using anti-WTAP antibody or rabbit IgG control were performed in THP-1-derived macrophages treated with 10 ng/mL IFN-β for 2 hours or left untreated. Binding between the promoters of *IFIT1*, *IFIT2*, *OAS1* and *OAS2* with WTAP were detected by qPCR assay. Ratios between ChIP-enriched DNA and input were shown (ChIP enrichment/input).

(C) ChIP experiments using anti-WTAP antibody or rabbit IgG control were performed in THP-1-derived macrophages transfected with *scramble* (*scr*) siRNA, *STAT1* siRNA or *PPP4* siRNA treated with 10 ng/mL IFN-β for 2 hours. Binding between the promoter regions of *IFIT1*, *IFIT2*, *OAS1* and *OAS2* with WTAP was detected by qPCR assay. Ratios between ChIP-enriched DNA and input were shown (ChIP enrichment/input).

(D) ChIP experiments using anti-WTAP antibody or rabbit IgG control were performed in control (GFP^{sgRNA}) and $WTAP^{sgRNA}$ #2 THP-1-derived macrophages with or without expression of Flag-tagged wild type (WT) WTAP, and its 5ST-D or 5ST-A mutants treated with 10 ng/mL IFN-β for 2 hours. Binding between the promoter regions of *IFIT1*, *IFIT2*, *OAS1* and *OAS2* with WTAP was detected by qPCR assay. Ratios between ChIP-enriched DNA and input were shown (ChIP enrichment/input).

(E) ChIP experiments using anti-WTAP antibody or rabbit IgG control were performed were performed in WT WTAP, 5ST-D or 5ST-A mutant-rescued $WTAP^{sgRNA}$ THP-1-derived macrophages treated with 10 ng/mL IFN-β along with 5% 1,6-hexanediol (hex) for 2 hours. Binding between the promoters of *IFIT1*, *IFIT2*, *OAS1* and *OAS2* with WTAP were detected by qPCR assay. Ratios between ChIP-enriched DNA and input were shown (ChIP enrichment/input).

(F) Schematic figure of IFN-β-induced phase transition of WTAP regulates the m^6A modification of ISG mRNAs.

All error bars, mean values ± SEM, P-values were determined by unpaired two-tailed Student's *t*-test of n = 3 independent biological experiments in (A-C). All error bars, mean values ± SEM, P-values were determined by one-way ANOVA test of n = 3 independent biological experiments in (D). All error bars, mean values ± SEM, P-values were determined by two-way ANOVA test of n = 3 independent biological experiments in (E).

Figure 1

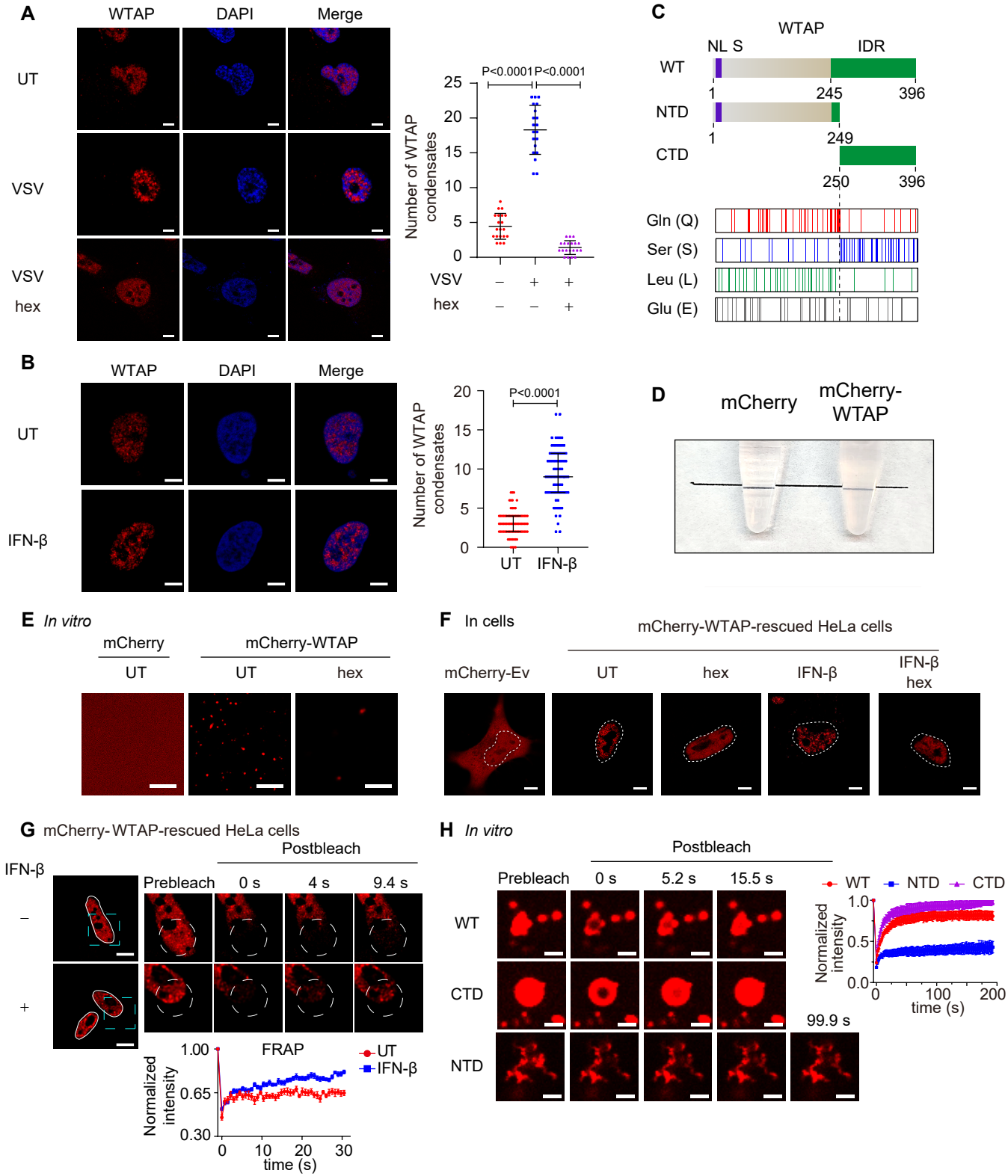
A
WTAP
DAPI
Merge
UT
VSV
VSV
hex
P<0.0001
P<0.0001
Number of WTAP condensates
25
20
15
10
5
0
VSV – + +
hex – – +
B
WTAP
DAPI
Merge
UT
IFN-β
P<0.0001
Number of WTAP condensates
20
15
10
5
0
UT
IFN-β
C
WTAP
NL S
IDR
WT
1
245
396
NTD
1
249
CTD
250
396
Gln (Q)
Ser (S)
Leu (L)
Glu (E)
D
mCherry
mCherry-WTAP
E In vitro
mCherry
mCherry-WTAP
UT
UT
hex
F In cells
mCherry-WTAP-rescued HeLa cells
mCherry-Ev
UT
hex
IFN-β
IFN-β hex
G mCherry-WTAP-rescued HeLa cells
Postbleach
IFN-β
–
+
Prebleach
0 s
4 s
9.4 s
FRAP
UT
IFN-β
Normalized intensity
1.00
0.65
0.30
0
10
20
30
time (s)
H In vitro
Postbleach
Prebleach
0 s
5.2 s
15.5 s
WT
CTD
NTD
99.9 s
WT
NTD
CTD
Normalized intensity
1.0
0.5
0.0
0
100
200
time (s)

Figure 2

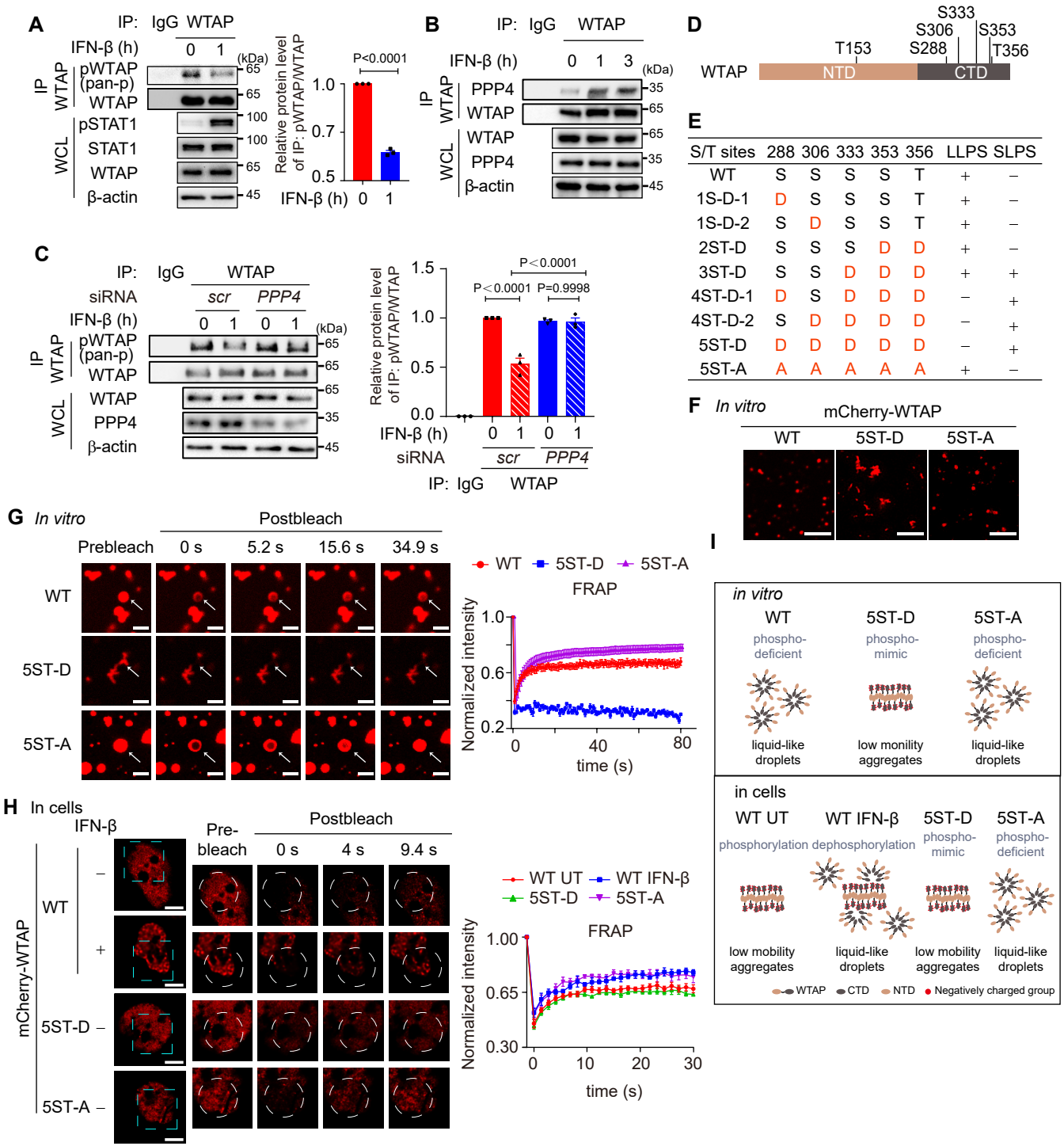
A
IP: IgG WTAP
IFN-β (h) 0 1
IP WTAP pWTAP (pan-p) WTAP
WCL pSTAT1 STAT1 WTAP β-actin
(kDa) 65 65 100 100 65 45
Relative protein level of IP: pWTAP/WTAP
P<0.0001
1.0 0.7 0.5
IFN-β (h) 0 1
B
IP: IgG WTAP
IFN-β (h) 0 1 3
IP WTAP PPP4 WTAP
WCL WTAP PPP4 β-actin
(kDa) 35 65 65 35 45
C
IP: IgG WTAP
siRNA scr PPP4
IFN-β (h) 0 1 0 1
IP WTAP pWTAP (pan-p) WTAP
WCL WTAP PPP4 β-actin
(kDa) 65 65 65 35 45
Relative protein level of IP: pWTAP/WTAP
P<0.0001 P<0.0001 P=0.9998
1.5 1.0 0.5 0.0
IFN-β (h) 0 1 0 1
siRNA scr PPP4
IP: IgG WTAP
D
S333 S306 S353 T153 S288 T356
WTAP NTD CTD
E
S/T sites 288 306 333 353 356 LLPS SLPS
WT S S S S T + –
1S-D-1 D S S S T + –
1S-D-2 S D S S T + –
2ST-D S S S D D + –
3ST-D S S D D D + +
4ST-D-1 D S D D D – +
4ST-D-2 S D D D D – +
5ST-D D D D D D – +
5ST-A A A A A A + –
F In vitro
mCherry-WTAP
WT 5ST-D 5ST-A
G In vitro
Postbleach
Prebleach 0 s 5.2 s 15.6 s 34.9 s
WT 5ST-D 5ST-A
WT 5ST-D 5ST-A
FRAP
Normalized intensity
1.0 0.6 0.2
0 40 80
time (s)
H In cells
IFN-β
Pre-bleach
Postbleach
0 s 4 s 9.4 s
mCherry-WTAP
WT – +
5ST-D –
5ST-A –
WT UT WT IFN-β 5ST-D 5ST-A
FRAP
Normalized intensity
1.00 0.65 0.30
0 10 20 30
time (s)
I
in vitro
WT phospho-deficient liquid-like droplets
5ST-D phospho-mimic low monility aggregates
5ST-A phospho-deficient liquid-like droplets
in cells
WT UT phosphorylation low mobility aggregates
WT IFN-β dephosphorylation liquid-like droplets
5ST-D phospho-mimic low mobility aggregates
5ST-A phospho-deficient liquid-like droplets
WTAP CTD NTD Negatively charged group

Figure 3

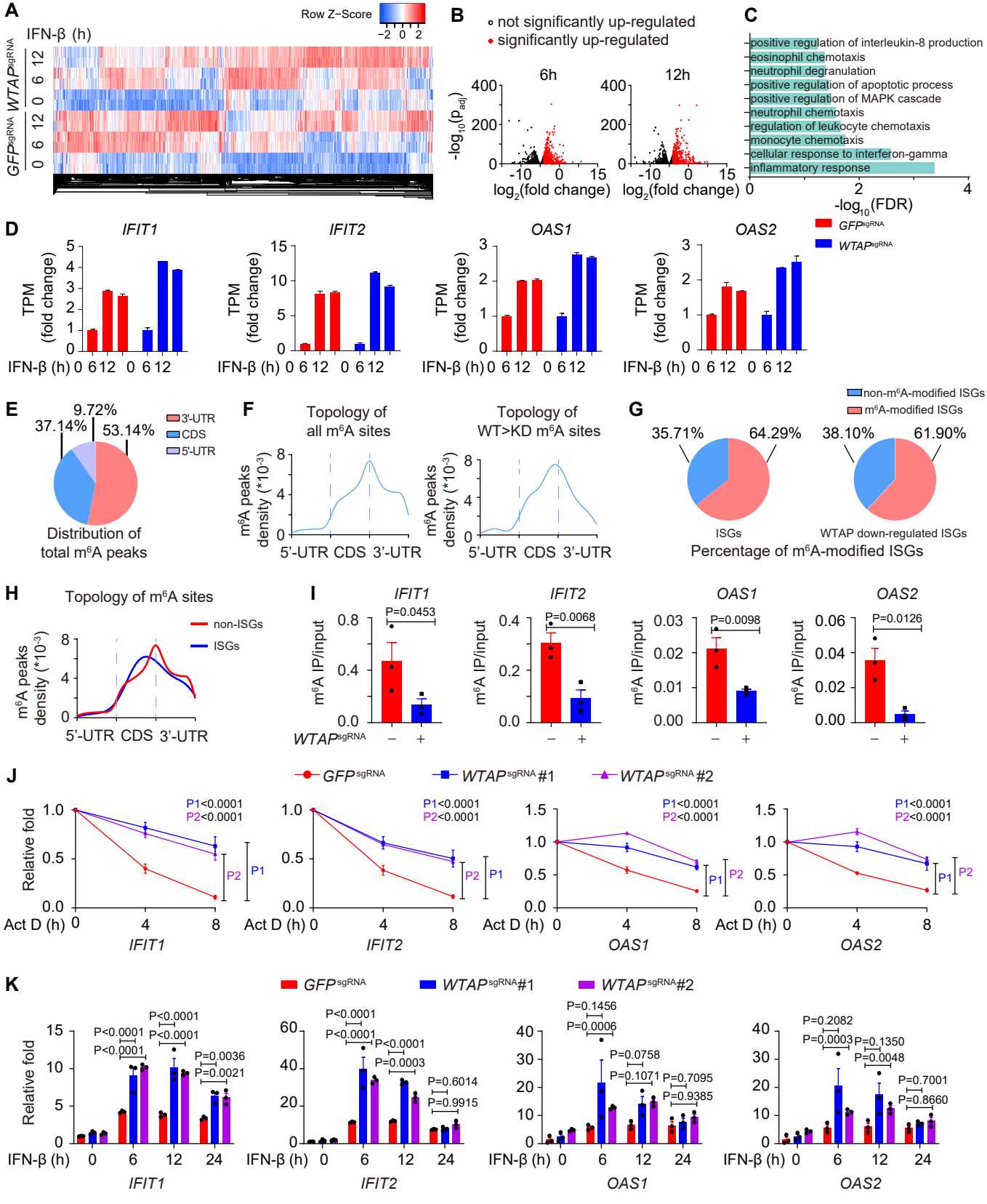
A
Row Z-Score
−2 0 2
IFN-β (h)
WTAP sgRNA
GFP sgRNA
0 6 12 0 6 12
B
not significantly up-regulated
significantly up-regulated
6h
12h
-log10(padj)
log2(fold change)
C
positive regulation of interleukin-8 production
eosinophil chemotaxis
neutrophil degranulation
positive regulation of apoptotic process
positive regulation of MAPK cascade
neutrophil chemotaxis
regulation of leukocyte chemotaxis
monocyte chemotaxis
cellular response to interferon-gamma
inflammatory response
-log10(FDR)
D
IFIT1
IFIT2
OAS1
OAS2
TPM (fold change)
IFN-β (h) 0 6 12 0 6 12
GFP sgRNA
WTAP sgRNA
E
9.72%
37.14%
53.14%
3'-UTR
CDS
5'-UTR
Distribution of total m6A peaks
F
Topology of all m6A sites
Topology of WT>KD m6A sites
m6A peaks density (*10-3)
5'-UTR CDS 3'-UTR
G
non-m6A-modified ISGs
m6A-modified ISGs
35.71%
64.29%
38.10%
61.90%
ISGs
WTAP down-regulated ISGs
Percentage of m6A-modified ISGs
H
Topology of m6A sites
non-ISGs
ISGs
m6A peaks density (*10-3)
5'-UTR CDS 3'-UTR
I
IFIT1
IFIT2
OAS1
OAS2
P=0.0453
P=0.0068
P=0.0098
P=0.0126
m6A IP/input
WTAP sgRNA
J
GFP sgRNA
WTAP sgRNA #1
WTAP sgRNA #2
P1<0.0001
P2<0.0001
P1
P2
Relative fold
Act D (h)
IFIT1
IFIT2
OAS1
OAS2
K
GFP sgRNA
WTAP sgRNA #1
WTAP sgRNA #2
P<0.0001
P=0.0036
P=0.0021
P=0.0003
P=0.6014
P=0.9915
P=0.1456
P=0.0006
P=0.0758
P=0.1071
P=0.7095
P=0.9385
P=0.2082
P=0.0003
P=0.1350
P=0.0048
P=0.7001
P=0.8660
Relative fold
IFN-β (h) 0 6 12 24
IFIT1
IFIT2
OAS1
OAS2

Figure 4

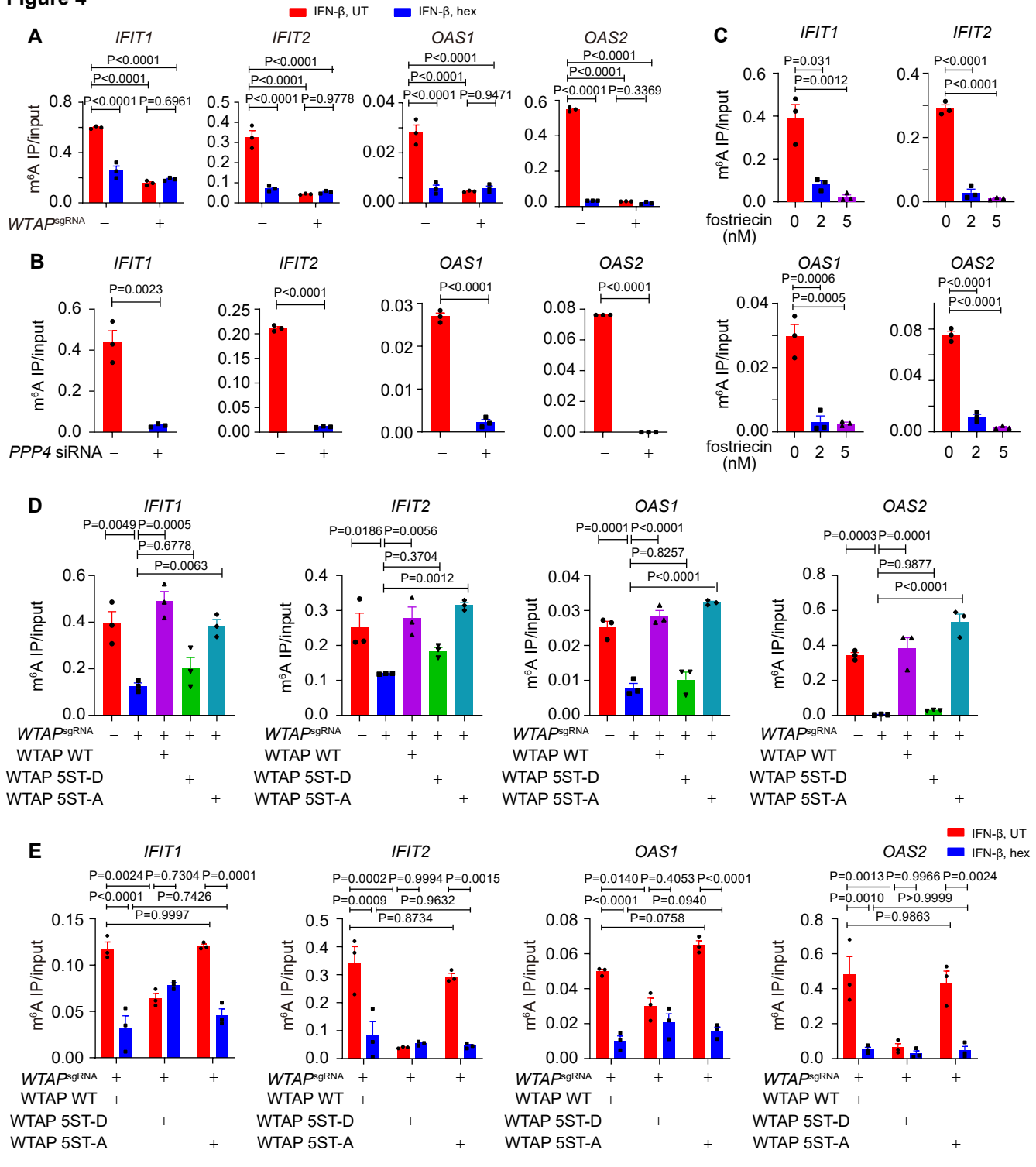
IFN-β, UT
IFN-β, hex
A
IFIT1
IFIT2
OAS1
OAS2
m6A IP/input
P<0.0001
P=0.6961
P=0.9778
P=0.9471
P=0.3369
WTAPsgRNA
B
P=0.0023
PPP4 siRNA
C
P=0.031
P=0.0012
P=0.0006
P=0.0005
fostriecin (nM)
D
P=0.0049
P=0.0005
P=0.6778
P=0.0063
P=0.0186
P=0.0056
P=0.3704
P=0.0012
P=0.0001
P=0.8257
P=0.0003
P=0.9877
WTAP WT
WTAP 5ST-D
WTAP 5ST-A
E
P=0.0024
P=0.7304
P=0.7426
P=0.9997
P=0.0002
P=0.9994
P=0.0015
P=0.0009
P=0.9632
P=0.8734
P=0.0140
P=0.4053
P=0.0940
P=0.0758
P=0.0013
P=0.9966
P=0.0024
P=0.0010
P>0.9999
P=0.9863

Figure 5

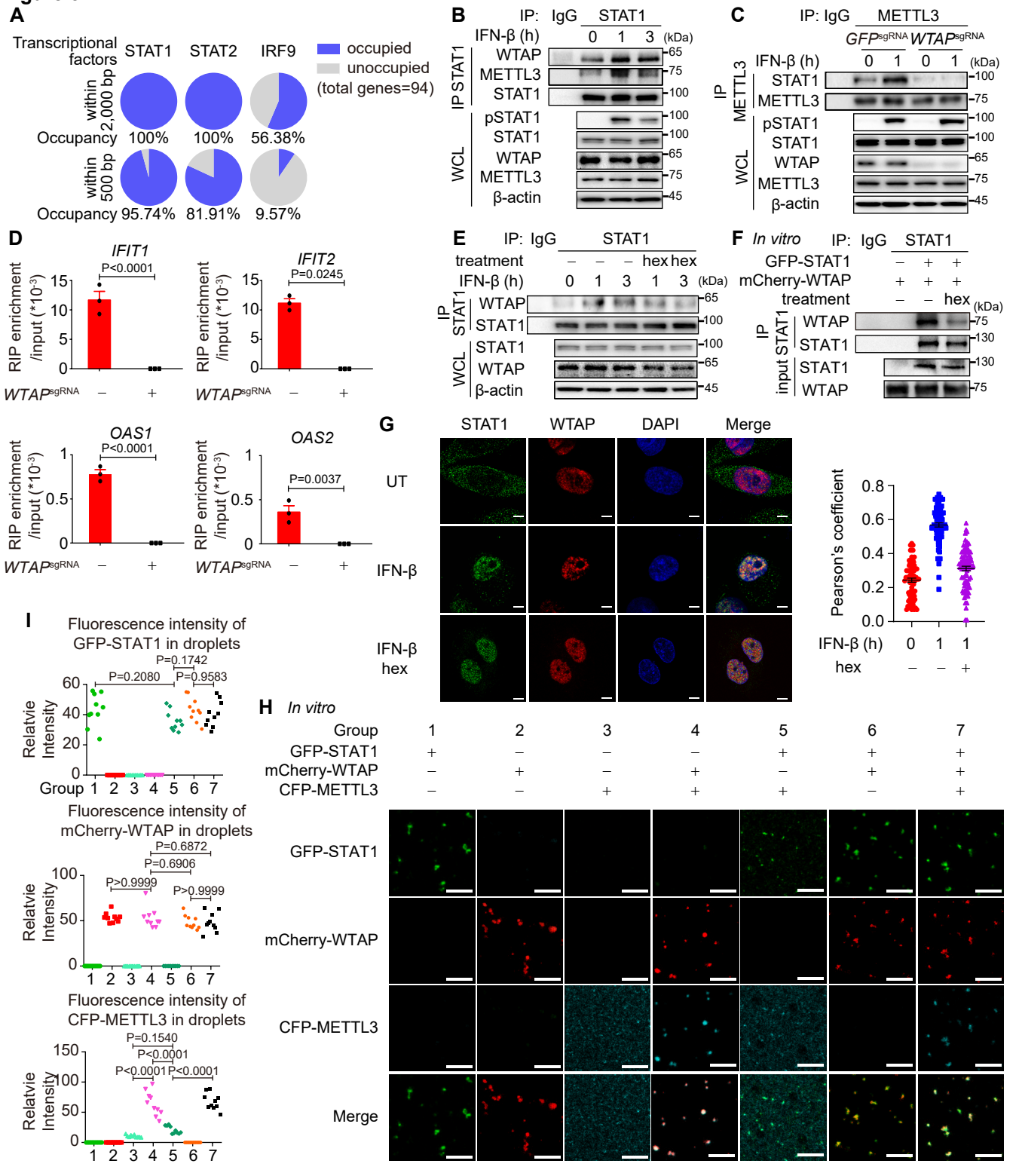
A
Transcriptional factors
STAT1
STAT2
IRF9
occupied
unoccupied
(total genes=94)
within 2,000 bp
Occupancy 100% 100% 56.38%
within 500 bp
Occupancy 95.74% 81.91% 9.57%
B
IP: IgG STAT1
IFN-β (h) 0 1 3 (kDa)
IP STAT1
WTAP
METTL3
STAT1
WCL
pSTAT1
STAT1
WTAP
METTL3
β-actin
C
IP: IgG METTL3
GFPsgRNA WTAPsgRNA
IFN-β (h) 0 1 0 1 (kDa)
IP METTL3
STAT1
METTL3
WCL
pSTAT1
STAT1
WTAP
METTL3
β-actin
D
IFIT1
P<0.0001
IFIT2
P=0.0245
OAS1
P<0.0001
OAS2
P=0.0037
RIP enrichment /input (*10-3)
WTAPsgRNA – +
E
IP: IgG STAT1
treatment – – – hex hex
IFN-β (h) 0 1 3 1 3 (kDa)
IP STAT1
WTAP
STAT1
WCL
STAT1
WTAP
β-actin
F In vitro
IP: IgG STAT1
GFP-STAT1 – + +
mCherry-WTAP + + +
treatment – – hex
IP STAT1
WTAP
STAT1
input
STAT1
WTAP
G
STAT1 WTAP DAPI Merge
UT
IFN-β
IFN-β hex
Pearson's coefficient
IFN-β (h) 0 1 1
hex – – +
I
Fluorescence intensity of GFP-STAT1 in droplets
P=0.1742
P=0.2080
P=0.9583
Relatvie Intensity
Group 1 2 3 4 5 6 7
Fluorescence intensity of mCherry-WTAP in droplets
P=0.6872
P=0.6906
P>0.9999
P>0.9999
Fluorescence intensity of CFP-METTL3 in droplets
P=0.1540
P<0.0001
P<0.0001
P<0.0001
H In vitro
Group 1 2 3 4 5 6 7
GFP-STAT1 + – – – + + +
mCherry-WTAP – + – + – + +
CFP-METTL3 – – + + + – +
GFP-STAT1
mCherry-WTAP
CFP-METTL3
Merge

Figure 6

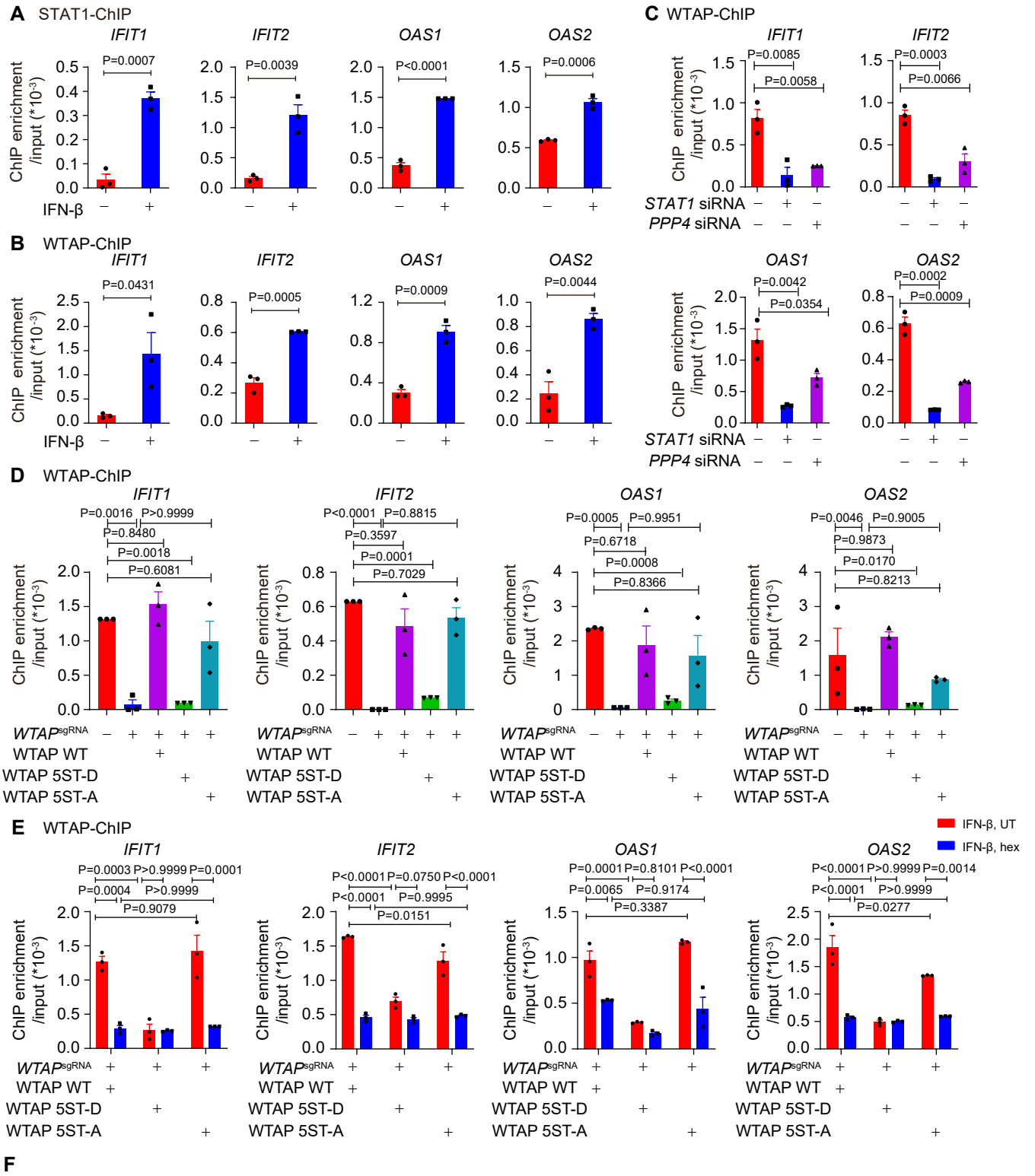
A STAT1-ChIP
IFIT1
IFIT2
OAS1
OAS2
P=0.0007
P=0.0039
P<0.0001
P=0.0006
ChIP enrichment /input (*10-3)
IFN-β
C WTAP-ChIP
P=0.0085
P=0.0058
P=0.0003
P=0.0066
STAT1 siRNA
PPP4 siRNA
B WTAP-ChIP
P=0.0431
P=0.0005
P=0.0009
P=0.0044
P=0.0042
P=0.0354
P=0.0002
P=0.0009
D WTAP-ChIP
P=0.0016
P>0.9999
P=0.8480
P=0.0018
P=0.6081
P<0.0001
P=0.8815
P=0.3597
P=0.0001
P=0.7029
P=0.0005
P=0.9951
P=0.6718
P=0.0008
P=0.8366
P=0.0046
P=0.9005
P=0.9873
P=0.0170
P=0.8213
WTAPsgRNA
WTAP WT
WTAP 5ST-D
WTAP 5ST-A
E WTAP-ChIP
IFN-β, UT
IFN-β, hex
P=0.0003
P>0.9999
P=0.0001
P=0.0004
P>0.9999
P=0.9079
P<0.0001
P=0.0750
P<0.0001
P<0.0001
P=0.9995
P=0.0151
P=0.0001
P=0.8101
P<0.0001
P=0.0065
P=0.9174
P=0.3387
P<0.0001
P>0.9999
P=0.0014
P<0.0001
P>0.9999
P=0.0277
F
IFN-β stimulation
PPP4
Phosphorylated
nucleus-translocated
STAT1
WTAP
IFN-β
METTL3
mRNA
Phosphate group
PPP4
STAT1
m6A modification
Dephosphorylation
Mobility enhanced
Gel-to-liquid
phase transition
ISG mRNAs
Aggregates
(low mobility)
Liquid condensates
(high mobility)
Promoter regions
of ISG